Supporting Information

Crystallographic visualization of C3-hydrocarbon-induced structural transformation and guest encapsulation within a flexible coordination network

Shao-Jie Qin,[#a] Mohana Shivanna,[#b] Mei-Yan Gao,[b] Cheng-Hua Deng,[b] Shi-Qiang Wang,[b] Dan Li,[a] Shao-Dan Fu,[a] Shuai Qiu,[a] Bai-Qiao Song*[a] and Qing-Yuan Yang*[c]

[a]College of Materials and Chemistry & Chemical Engineering, Chengdu University of Technology, Chengdu 610059, China

[b]Department of Chemical Sciences and Bernal Institute, University of Limerick, Limerick V94 T9PX, Republic of Ireland

[c]School of Chemical Engineering and Technology, Xi'an Jiaotong University, Xi'an 710049, China

Table of contents

1. Materials and Synthesis

The crystalline samples were synthesized using previously reported methods.[1] The ligand 1,4-Bis(1-imidazolyl)benzene (L) was synthesized according to the literature method.[2] Other reagents and solvents were commercially available and used without further purification.

$[Cu(SiF_6)(L)_2]\cdot xMeOH\cdot yH_2O$ (SIFSIX-23-Cu-α). A 5 mL water solution containing $CuSiF_6\cdot H_2O$ (22 mg, 0.1 mmol) was placed in the bottom of a glass tube, on which 5 mL mixed MeOH/water (1:1) buffer was layered. Finally, a 5 mL MeOH solution containing bi-imidazolyl ligand (42 mg, 0.2 mmol) was carefully layered on the top. After several days, purple needle/rod/block shaped crystals were formed on the glass wall. The crystals were collected after three weeks to optimize the yield. The harvested crystals were washed with MeOH before drying (Yield: ca. 60%).

Single crystal loaded with gas molecules at 298 K. SIFSIX-23-Cu⊃gas. First, good quality single crystals were put into the sample tube of Micromeritics 3Flex instrument which was activated at 100 °C under high vacuum for at least 3 hours. Second, the activated sample tube was put onto the port of Micromeritics 3Flex and specific C3 gas (C_3H_4, C_3H_6, C_3H_8) was filled into the tube with a controlled gas pressure of 1 bar, which was maintained for about 3 hours to fulfil the adsorption. Third, after completion of the adsorption, the tube was removed from the instrument (the sample inside the tube still under C3 gas atmosphere) and the crystal sample was quickly poured onto the microscope slide and good quality single crystal was picked and transferred immediately to the SCXRD diffraction instrument (The instrument's temperature was preset to 150 K). During the processing procedure, the microscope slide remained under the protection of C3 gas atmosphere via a pipe connected to a gas cylinder.

2. Single-crystal X-ray diffraction measurements (SCXRD)

SCXRD of crystals loaded with gas molecules at 298 K

SIFSIX-23-Cu⊃gas:

For all the gas-loaded single crystals, **SIFSIX-23-Cu⊃gas**, in order to avoid the escape of gas molecules and the interference of water in air, the picked suitable single crystals were dipped immediately in paraffin oil and quickly mounted on the instrument and kept under liquid N_2 flow at 150 K. The refection data were collected on a Bruker Quest diffractometer equipped with a CMOS detector and IμS microfocus X-ray source (Cu-Kα, λ = 1.54178 Å; Mo-Kα, λ = 0.71073 Å).

In all cases, data were indexed, integrated and scaled in APEX3.[3] Absorption correction was performed by multi-scan method using in SADABS.[4] Space group was determined using XPREP[5] implemented in APEX3. Structures were solved using intrinsic phasing method (SHELXT)[6] and refined on F^2 using nonlinear least-squares techniques with SHELXL[7] programs incorporated in OLEX2 graphical user interface.[8] Anisotropic thermal parameters were applied to all non-hydrogen atoms of the host framework. The hydrogen atoms were placed in calculated positions using riding models.

For **SIFSIX-23-Cu⊃C_3H_4**, totally three different types of gas molecules (C_3H_4-I, C_3H_4-II and C_3H_4-III) were identified unequivocally. C_3H_4-III was refined anisotropically without any molecular geometric constrains and the thermal parameter was reasonable. The refined occupancy of C_3H_4-III was close to 1. C_3H_4-I and C_3H_4-II could not appear simultaneously due to the short intermolecular C···C separations (< 2.2 Å). We fixed the occupancies of these two non-coexisting molecules to be 0.5:0.5, and bond lengths constrains (DFIX) and thermal parameters constrains (SIMU and ISOR) were applied to C_3H_4-I and both, respectively. Consequently, there is a 0.3 molecule difference between the adsorption results and the crystal data, which is possibly ascribed to the surface adsorption of the sample.

For **SIFSIX-23-Cu⊃C_3H_6**, total three types of gas molecules (C_3H_6-I, C_3H_6-II and C_3H_6-III) were discovered from the difference electron density map. C_3H_6-I was refined anisotropically without any molecular geometric constrains and the refined occupancy was close to 1. For C_3H_6-II and C_3H_6-III, the geometric constrains (DFIX)

and thermal parameters constrains (SIMU and ISOR) were applied to these two molecules when refinements were conducted, due to the poor data set mainly arising from twinning (single crystal particle may fracture into small parts when gas induced the structure expansion from nonporous status to narrow pore form). Similarly, the accurate electron counts in the cavity could not be determined using SQUEEZE.[9] Therefore, the occupancies of C_3H_6-II and C_3H_6-III were fixed at values which could improve the refinement results. But based on the adsorption isotherms of C_3H_6, three types of gas molecules should be captured into the narrow-pore phase, which matched with the single crystal data. Although the molecules numbers (occupation) in the channel could not be accurately calculated, the most valuable information we got here was the position of the gas molecules which had significant importance to evaluate the host-guest interactions.

For **SIFSIX-23-Cu⊃C_3H_8**, total two types of gas molecules (C_3H_8-I and C_3H_6-II) were identified. Due to the poor data set mainly arising from twinning (single crystal particle may fracture into small parts when gas induced the structure expansion from nonporous status to narrow pore form), the geometric constrains (DFIX) and thermal parameters constrains (SIMU and ISOR) were applied to these two molecules when refinements were conducted. Similarly, the accurate electron counts in the cavity could not be determined using SQUEEZE. Hence, the occupancies of C_3H_8-I and C_3H_8-II were fixed at values which could improve the refinement results. But based on the adsorption isotherms of C_3H_8, two types of gas molecules should be captured into the narrow-pore phase, which matched with the single crystal data. Although the molecules numbers in the channel could not be accurately calculated, the most valuable information we got here was the position of the gas molecules which had significant importance to evaluate the host-guest interactions. It is worth to mention that the positions of C_3H_8-I and C_3H_8-II are similar to those of C_3H_6-I and C_3H_6-III, in accord with the similar adsorption isotherm shapes for C_3H_6 and C_3H_8 (the gate opening pressures were close to each other but the uptakes were different), validating the reliability of single crystal data.

We performed gas loading (even increasing the equilibrium adsorption time) and

SCXRD experiments for multiple times using different crystals for each gas species (298 K), and the results showed subtle difference between different batches, confirming the reliability of the crystal data. For each gas, the unit cell parameters obtained immediately after the crystal mounted is the same as those determined at the end of data collection, confirming that no structural changes occurred during the data collection stage.

The void volumes (excluding entrapped gas molecules) in the crystal cells were calculated using the program PLATON.[10] Due to the disorder of organic bi-imidazolyl ligands in **SIFSIX-23-Cu-α**, the accessible void volume has been calculated considering an average value from each disordered part. Crystallographic data and structural refinement information are listed in Tables S1. Crystallographic data for the structures reported in this paper have been deposited with the Cambridge Crystallographic Data Centre as **CCDC** number, 2034435 (**SIFSIX-23-Cu⊃C_3H_4**), 2044415 (**SIFSIX-23-Cu⊃C_3H_6**) and 2044416 (**SIFSIX-23-Cu⊃C_3H_8**) (available free of charge, on application to the CCDC, 12 Union Rd., Cambridge CB2 1EZ, U.K.; e-mail deposit@ccdc.cam.ac.uk).

3. Low-pressure gas adsorption measurements

The sorption isotherms for C3 hydrocarbons at different temperatures (273 K and 298 K) were measured using Micromeritics 3 Flex surface area and pore size analyser. A Julabo temperature controller was used to maintain a constant temperature in the bath through the duration of the experiment. Before gas sorption experiment, the freshly prepared sample of **SIFSIX-23-Cu** was placed in the quartz tube and degassed under high vacuum at 100 ^{o}C for 2 hours on a Smart VacPrep instrument to remove the remnant solvent molecules.

4. Thermogravimetric analysis (TGA)

Thermogravimetric analyses (TGA) were performed under N_2 using a TA Instruments Q50 system. Samples were loaded into aluminium sample pans and heated at 5 K min^{-1} from room temperature to 550 ^{o}C.

5. Powder X-ray diffraction measurements (PXRD)

Powder X-ray diffraction patterns were recorded on a PANalytical X'Pert MPD Pro (Cu Ka, λ = 1.5418 Å) with a 1D X'Celerator strip detector. Experiments were conducted in continuous scanning mode with the goniometer in the theta-theta orientation. Incident beam optics included the Fixed Divergences slit with anti-scatter slit PreFIX module, with a 1/8° divergence slit and a 1/4° anti-scatter slit, as well as a 10 mm fixed incident beam mask and a Soller slit (0.04 rad). Divergent beam optics included a P7.5 anti-scatter slit, a Soller slit (0.04 rad), and a Ni β filter. The data were collected in the range of 2θ = 3-50. Raw data was then evaluated using the X'Pert HighScore Plus™ software V 4.1 (PANalytical, The Netherlands).

6. Calculation of adsorption enthalpies

The isosteric adsorption enthalpy for C3 hydrocarbons were calculated using the single component gas adsorption isotherms collected at 273 and 298 K. The adsorption isotherms were first fitted with the dual-site Langmuir-Freundlich (DSLF) equation,[11] subsequently the adsorption enthalpy (Q_{st}) was calculated using Clausius-Clapeyron method[12]. The DSLF equation is given as:

$$n(P) = \frac{n_{m1} b_1 P^{t_1}}{1 + n_{m1} b_1 P^{t_1}} + \frac{n_{m2} b_2 P^{t_2}}{1 + n_{m2} b_2 P^{t_2}}$$

In this equation, n is the amount adsorbed per mass of material (mmol/g), P is the total pressure (kPa) of the bulk gas at equilibrium with the adsorbed phase, $nm1$ and $nm2$ are the saturation uptakes (mmol/g) for sites 1 and 2, $b1$ and $b2$ are the affinity coefficients (kPa^{-1}) for sites 1 and 2, and $t1$ and $t2$ represent the deviations from the ideal homogeneous surface (unit-less) for sites 1 and 2. The parameters that were obtained from the fitting for **SIFSIX-23-Cu** can be found in supporting figures.

The obtained parameters were used to calculate Q_{st} in the range of adsorption capacity through the Clausius-Clapeyron equation, which is as follows:

$$Q_{st} = -R\left[\frac{\partial lnP}{\partial\left(1/T\right)}\right]_n$$

Where T is temperature (in K) and R is the ideal gas constant (8.314 J mol^{-1} K^{-1}). Integrating this equation gives:

$$(\ln P)_n = -\left(\frac{Q_{st}}{R}\right)\left(\frac{1}{T}\right) + C$$

Where *C* is a constant. As in our case only isotherms at two different temperatures were used to calculated, the express for Q_{st} can be simplified as following:

$$Q_{st} = \left[RT_1T_2\frac{lnP_2 - lnP_1}{T_2 - T_1}\right]_n$$

The values of *P* at a given *n* for each *T* can be interpolated from the DSLF fitted equation.

7. Breakthrough experiments

In typical breakthrough experiments, ~0.50 g of finely grinded sample was first placed in quartz tubing (8 mm diameter) to form fixed bed. Then, the adsorbent bed was purged under a 20 cm^3 min^{-1} flow of He gas at 100 °C for 3 hours to activate the sample prior to breakthrough experiments. Upon cooling to room temperature, a binary gas mixture (C_3H_4/C_3H_6, 40:60 or 10:90, v/v) or a ternary gas mixture ($C_3H_4/C_3H_6/C_3H_8$, 10:40:50, v/v/v) at a total flow rate of 1 ml/min was introduced to the activated column bed to perform breakthrough experiments at 25 °C and 1 bar. The outlet composition was continuously monitored by a gas chromatography (Shimadzu GC2030 with an FID detector) until complete breakthrough was achieved. Once the breakthrough experiment finished, the inlet gas was immediately switched from hydrocarbon mixture to He flow at a flow rate of 20 ml/min, to desorb the adsorbed gas at 25 °C. After a period of time, the packed column bed was heated to 100 ºC to check the desorption level and increase the desorption rate. The desorption curves were also monitored and recorded via GC as above. The packed column bed was regenerated at 100 ºC with constant He flow (20 cm^3 min^{-1}) over night to ensure complete sample regeneration.

8. Supporting Figures

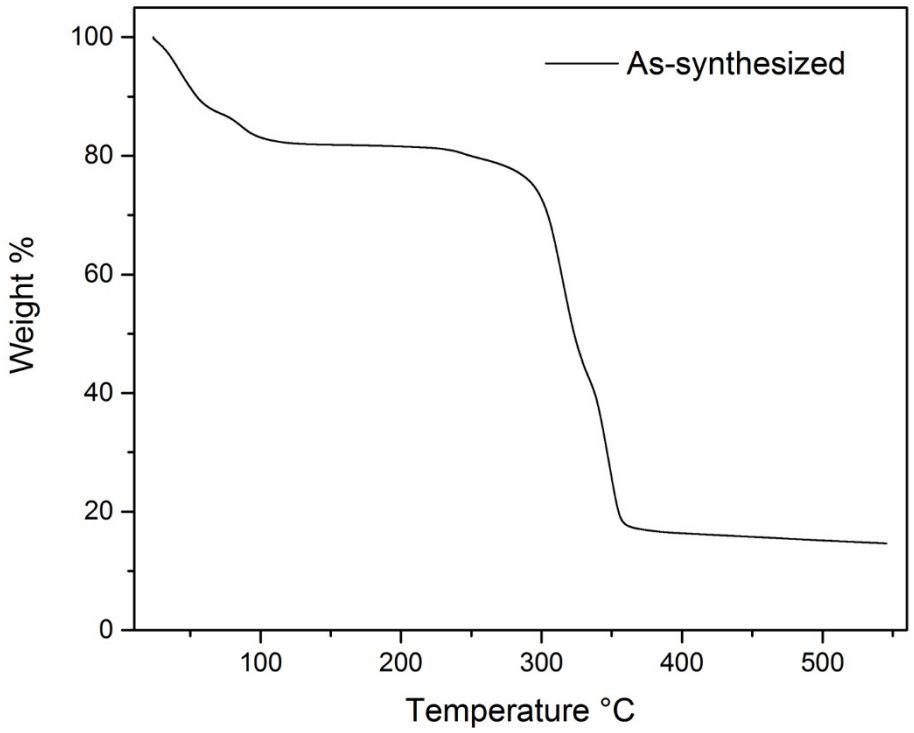

Figure S1. TGA curve of as-synthesized **SIFSIX-23-Cu**.

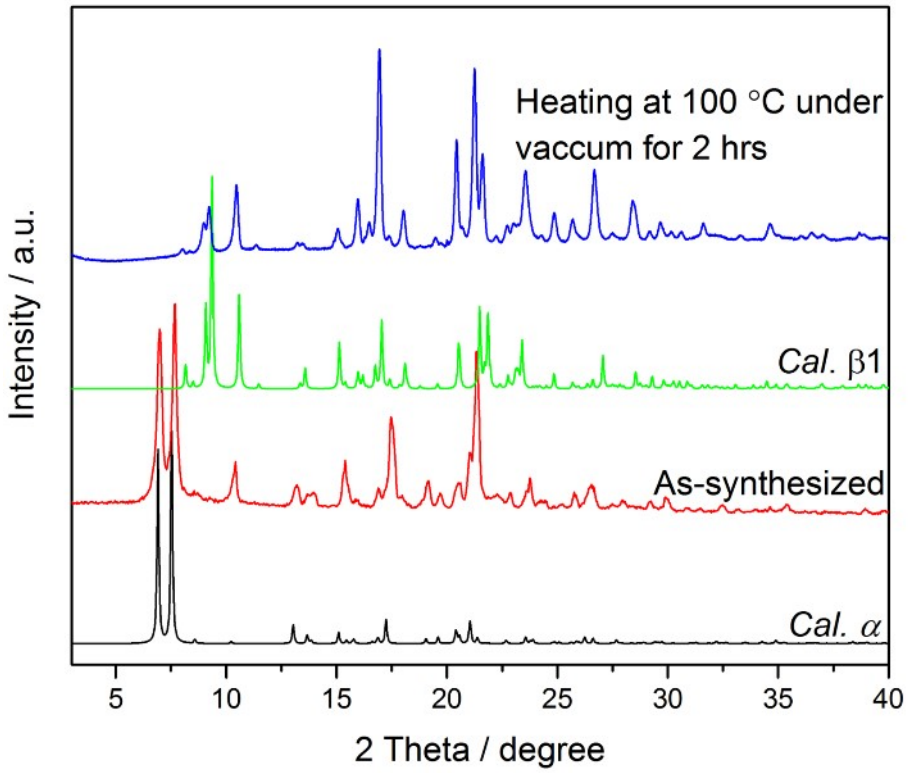

Figure S2. PXRD patterns of as-synthesized and activated samples of **SIFSIX-23-Cu**. Note: as-

synthesized wet sample was immediately measured before drying to exclude the phase transformation induced by guest release.

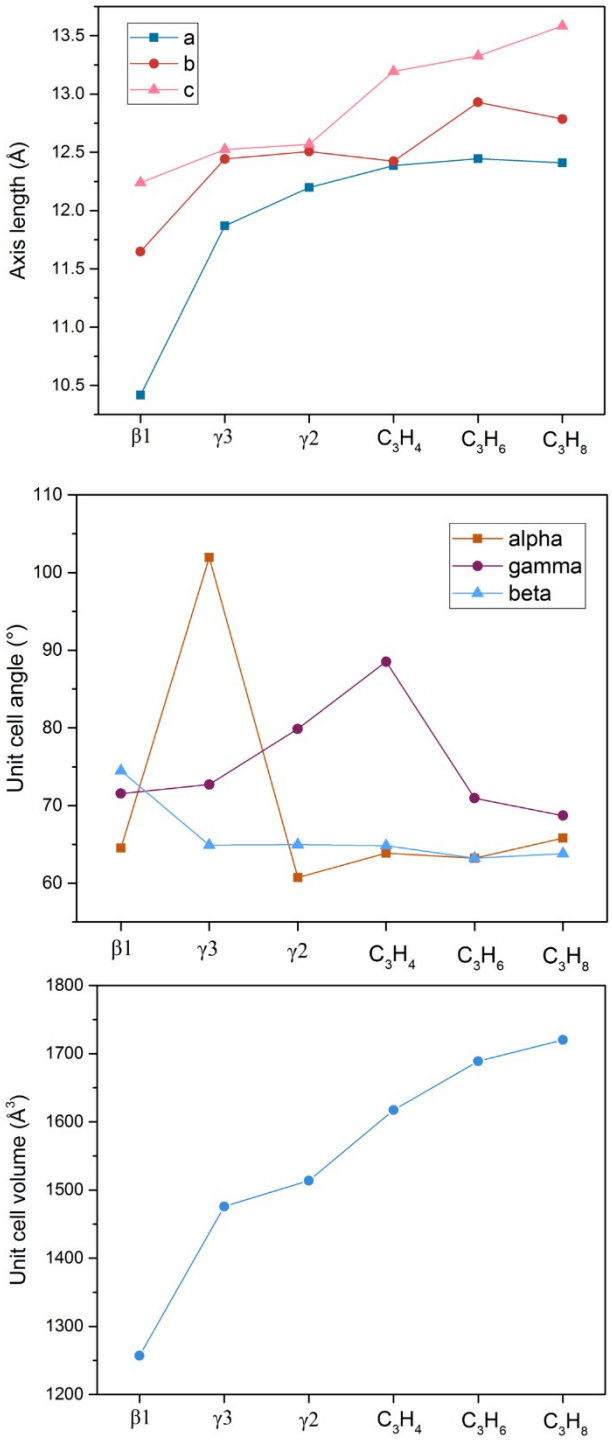

Figure S3. Comparison of unit cell parameters of different pahses: axis (top), angle (middle) and volume (bottom). The name of gas-loaded structures have been represented as the name of gas species in the channels for short.

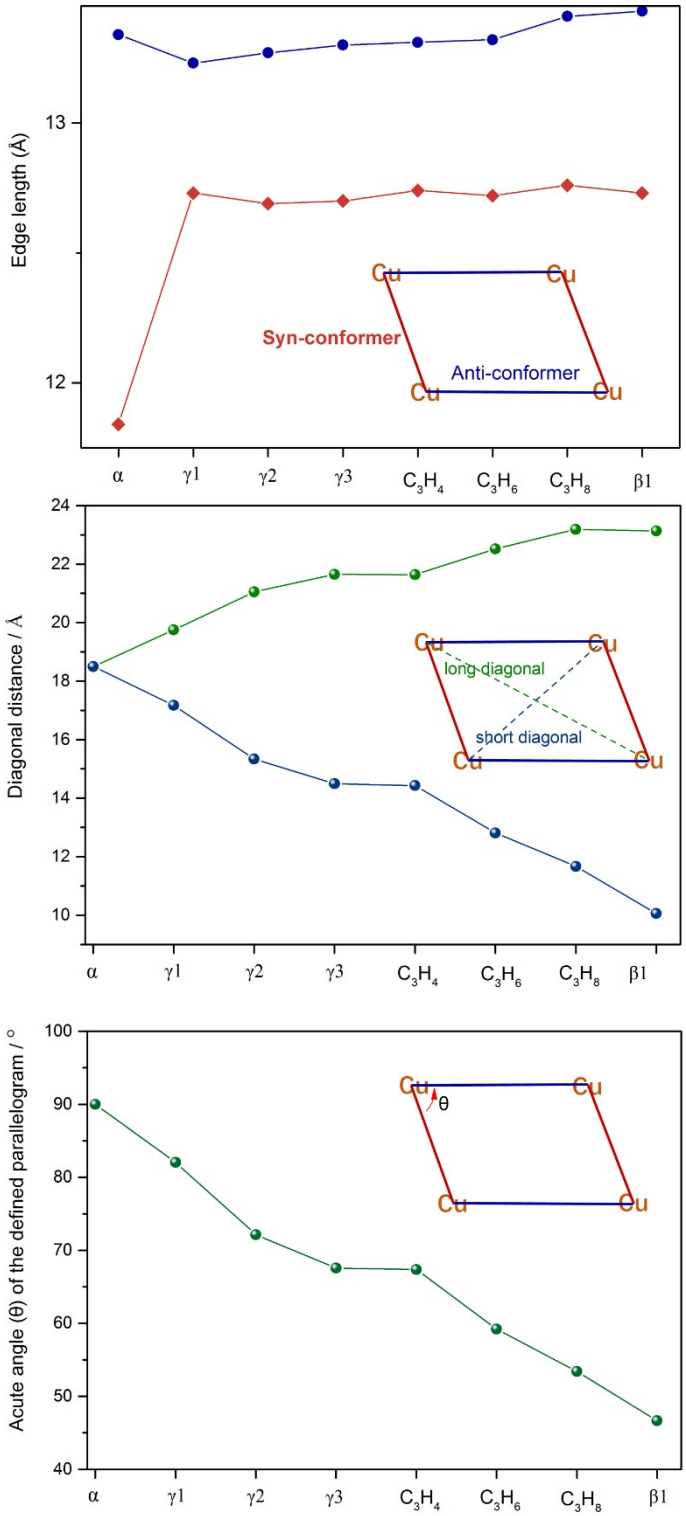

Figure S4. The edge length (top), diagonal distance (middle) and acute angle (θ) of simplified CuL_2 **sql** net in different phases.

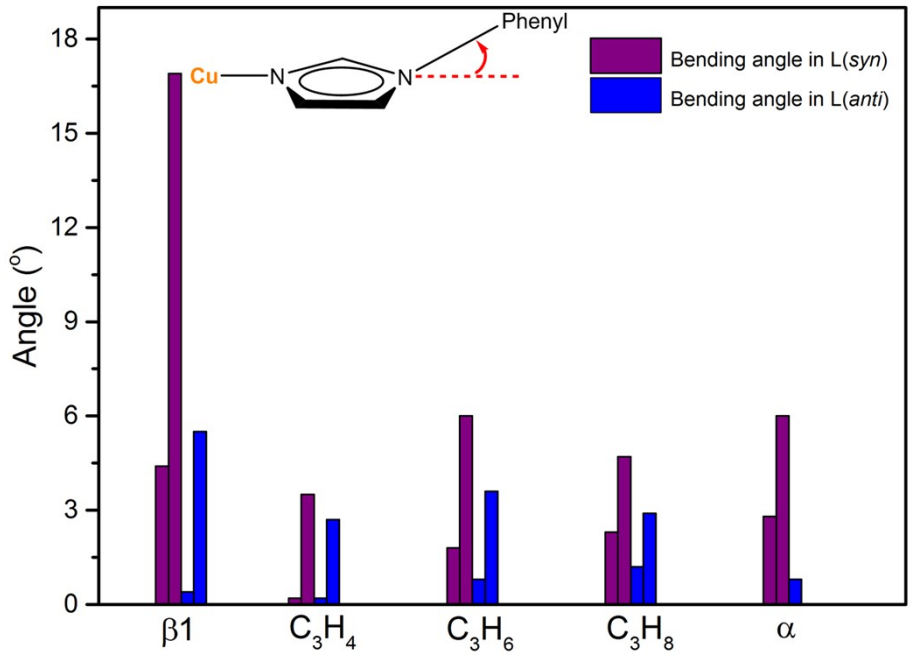

Figure S5. Angles between C_{phenyl}-$N_{imidazolyl}$ covalent bond and imidazolyl plane which quantify the bending of ligand scaffold. The name of gas-loaded structures have been represented as the name of gas species in the channels for short.

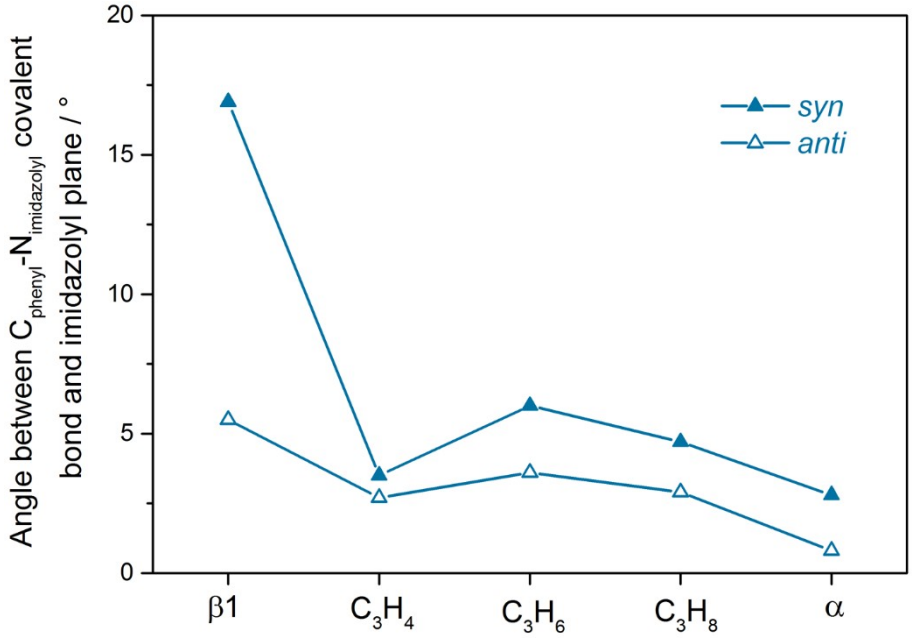

Figure S6. The maximum angles between C_{phenyl}-$N_{imidazolyl}$ covalent bond and imidazolyl plane in L(*syn*) (blue solid triangle) and L(*anti*) (blue hollow triangle) in each phase, quantifying the bending level of ligands. The name of gas-loaded structures have been represented as the name of gas species in the channels for short.

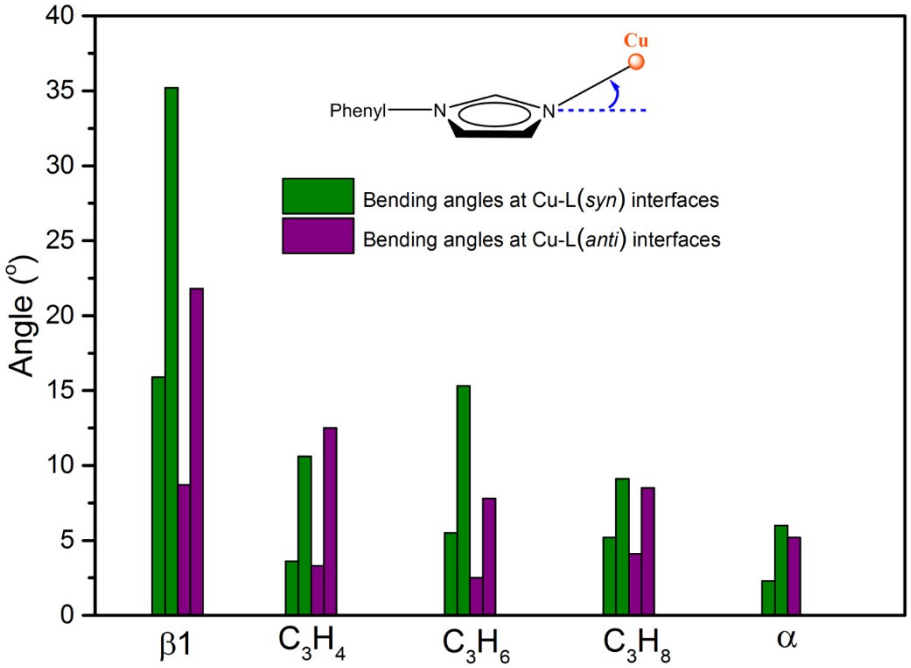

Figure S7. Angles between Cu-N coordination bond and imidazolyl plane which quantify the bending at metal-ligand interfaces. The name of gas-loaded structures have been represented as the name of gas species in the channels for short.

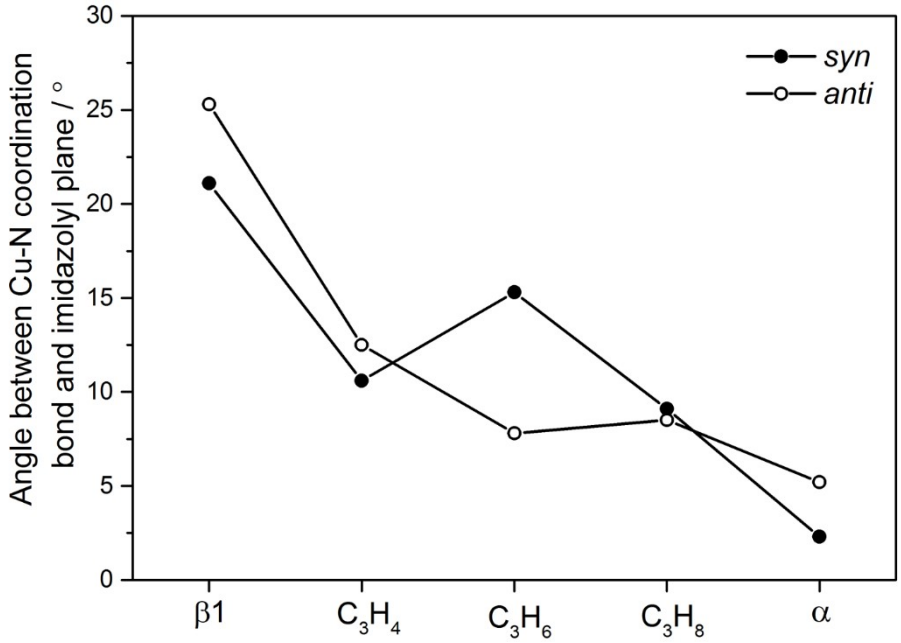

Figure S8. The maximum angles between Cu-N coordination bond and imidazolyl plane, quantifying the bending degree of Cu-imidazolyl junction between Cu ions and L(*syn*) (black solid circle) and L(*anti*) (black hollow circle) in each phase. The name of gas-loaded structures have been represented as the name of gas species in the channels for short.

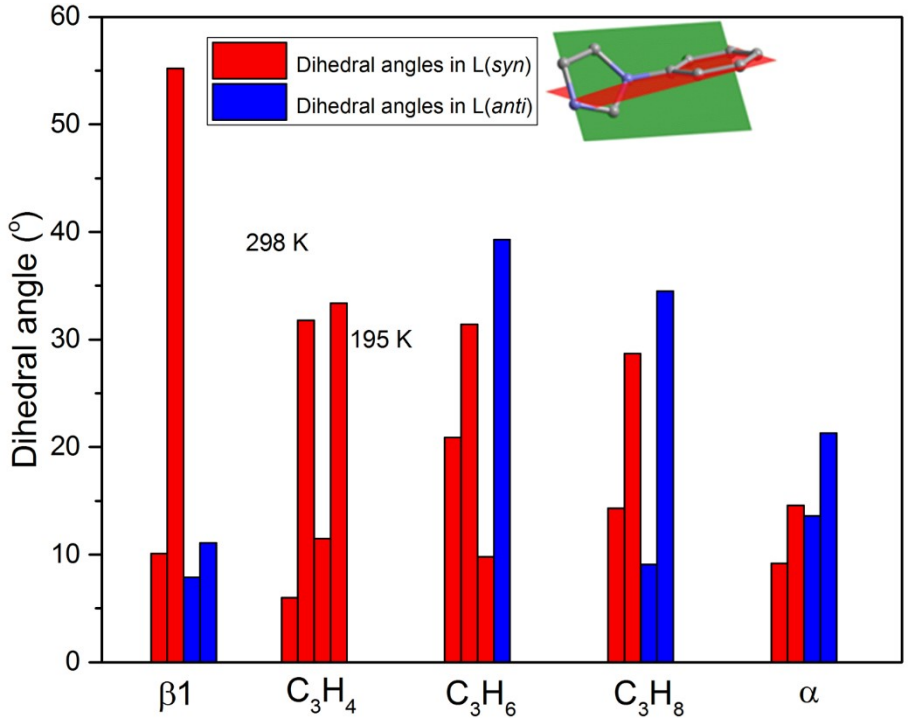

Figure S9. Dihedral angles between imidazolyl plane and phenyl plane, quantifing the ligand rotation. The name of gas-loaded structures have been represented as the name of gas species in the channels for short.

Figure S10. The maximum angles between imidazolyl plane and phenyl plane in L(*syn*) (blue solid triangle) and L(*anti*) (blue hollow triangle) in each phase, quantifying ligand rotation. The name of gas-loaded structures have been represented as the name of gas species in the channels for short.

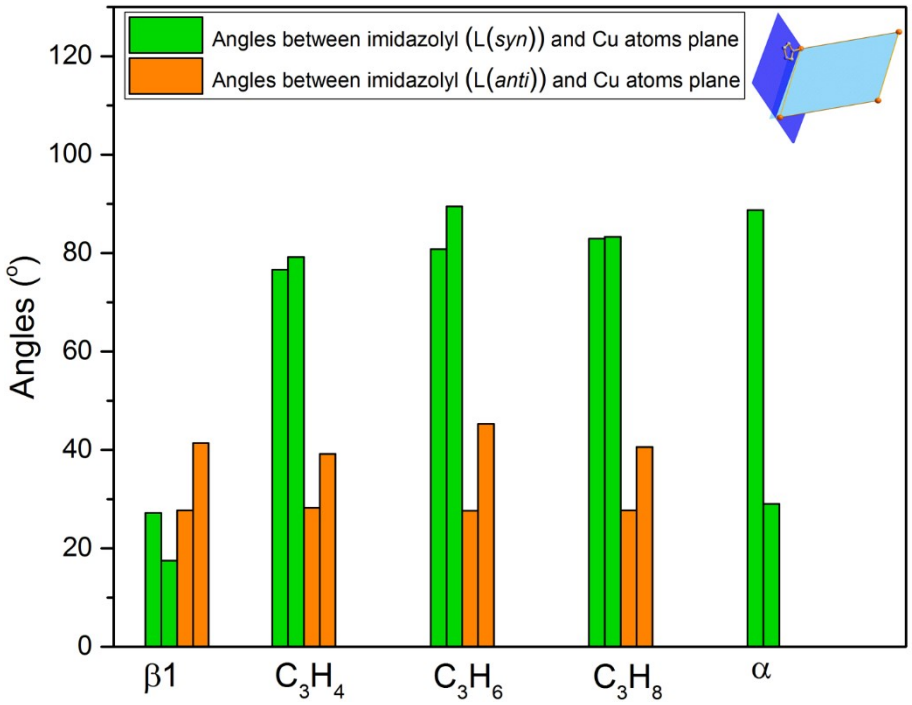

Figure S11. The maximum angles between imidazolyl plane and phenyl plane in each phase, quantifying ligand rotation. The name of gas-loaded structures have been represented as the name of gas species in the channels for short.

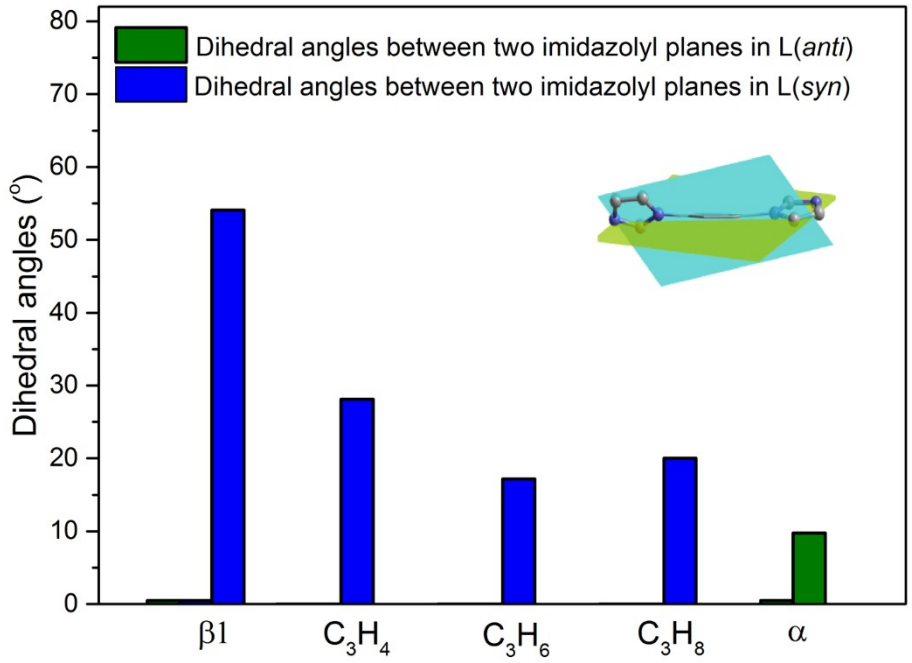

Figure S12. Dihedral angles between imidazolyl planes. The name of gas-loaded structures have been represented as the name of gas species in the channels for short.

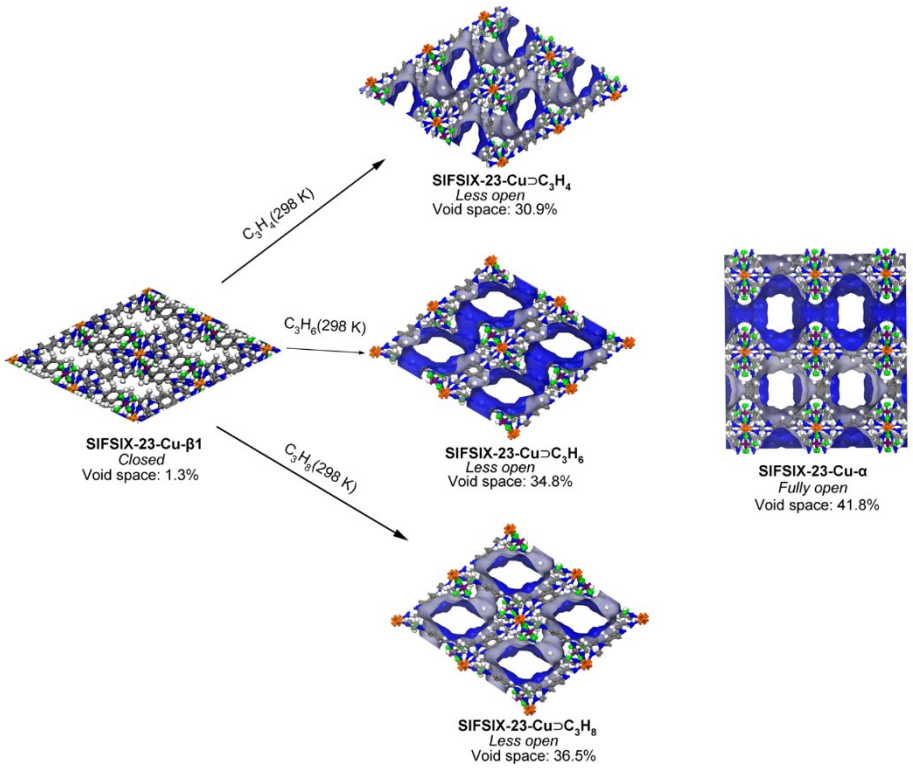

Figure S13. View of the 3D frameworks and channel structures of **SIFSIX-23-Cu-α**, **SIFSIX-23-Cu-β1**, **SIFSIX-23-Cu⊃C_3H_4**, **SIFSIX-23-Cu⊃C_3H_6** and **SIFSIX-23-Cu⊃C_3H_8**. The gas molecules entrapped in the channels have been excluded for calculations.

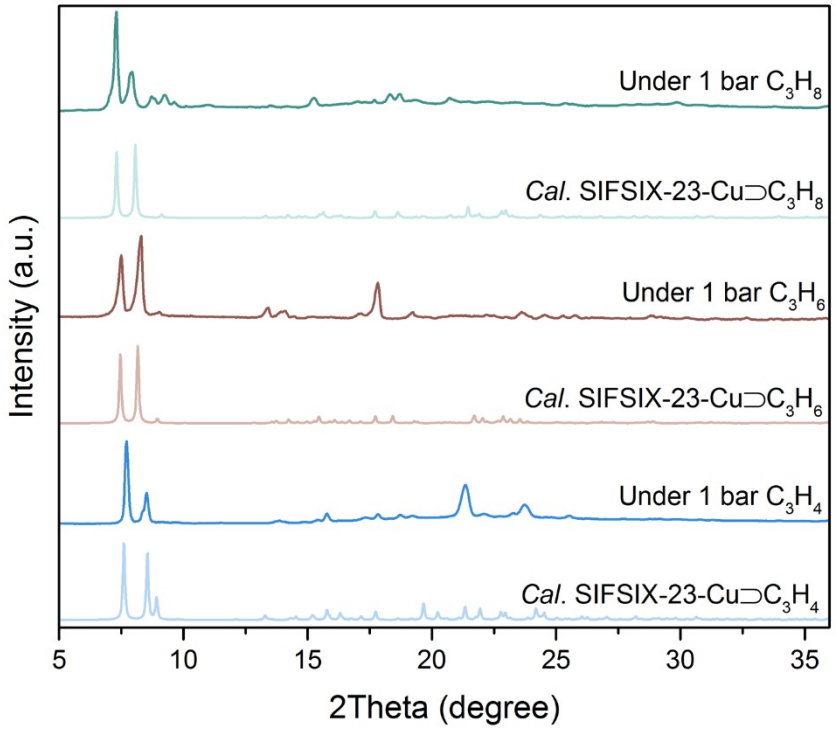

Figure S14. The PXRD patterns of **SIFSIX-23-Cu-β**1 under 1 bar of each C3 gas. The PXRD patterns calculated from the C3-loaded single crystal structures were provided for comparison.

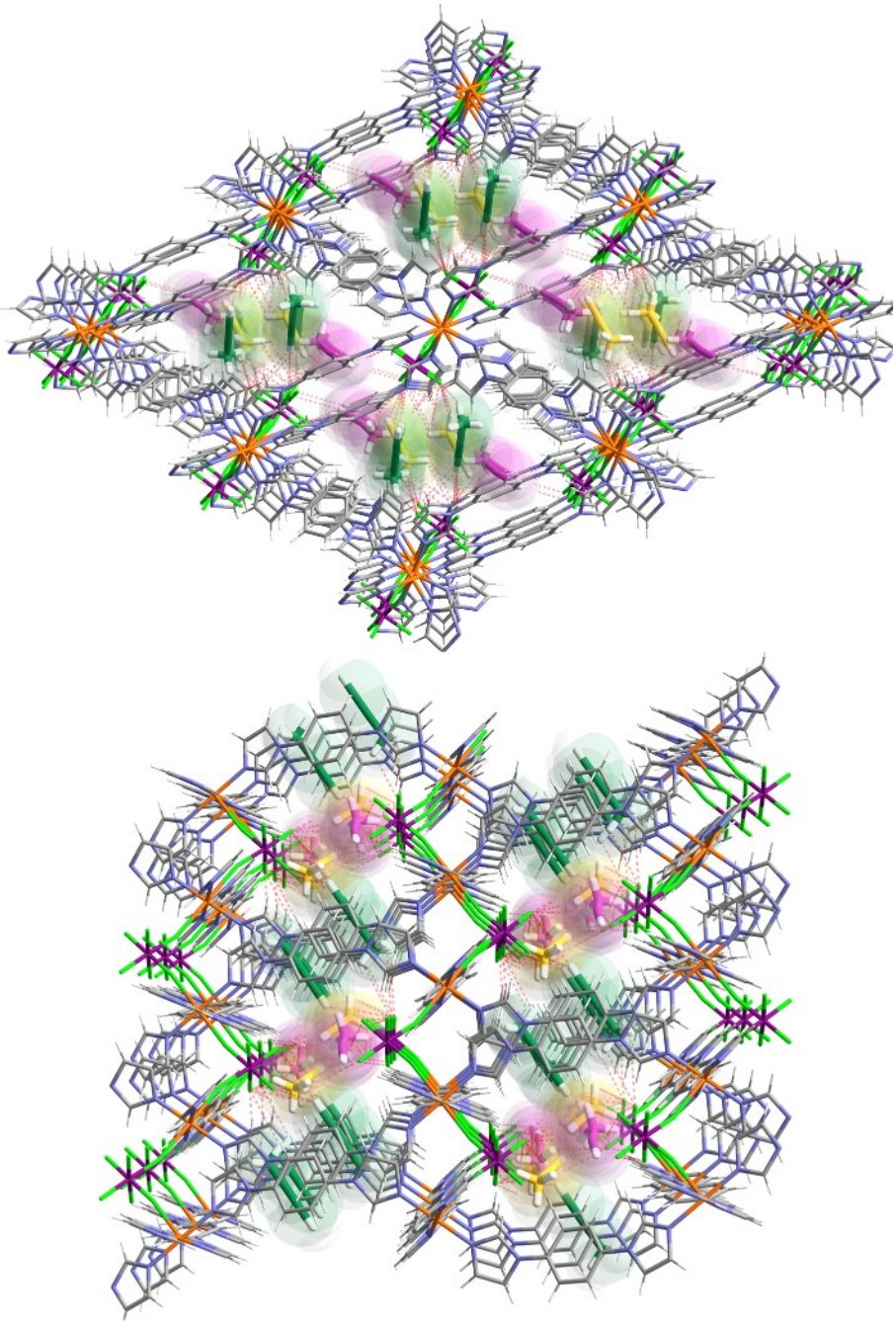

Figure S15. (Top) Top view and side view (bottom) of the periodic arrangement of C_3H_4 molecules in **SIFSIX-23-Cu⊃C_3H_4**.

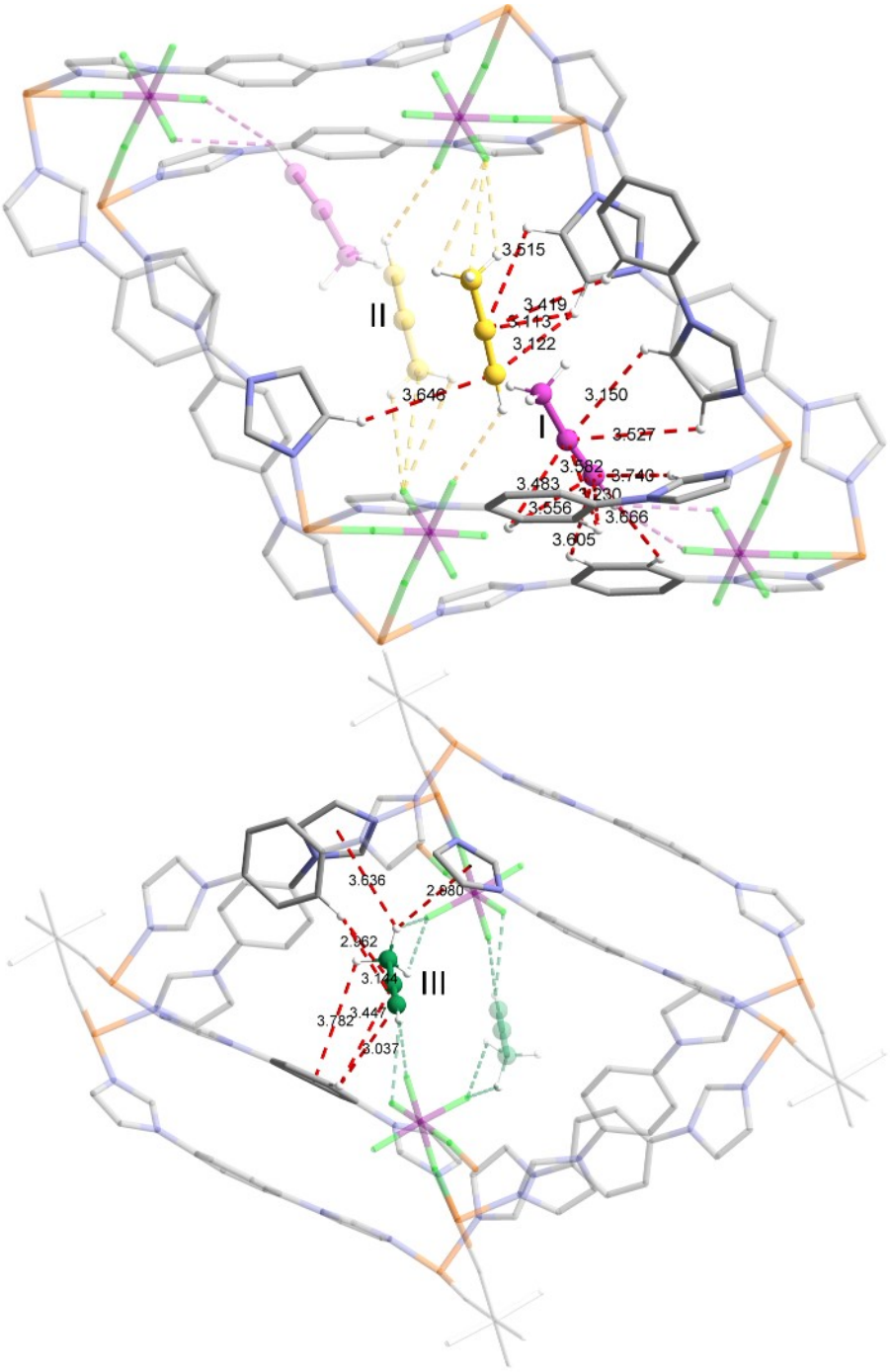

Figure S16. Other host-guest interactions stabilizing the C_3H_4 molecules (e.g., van der Waals forces) in **SIFSIX-23-Cu⊃C_3H_4**.

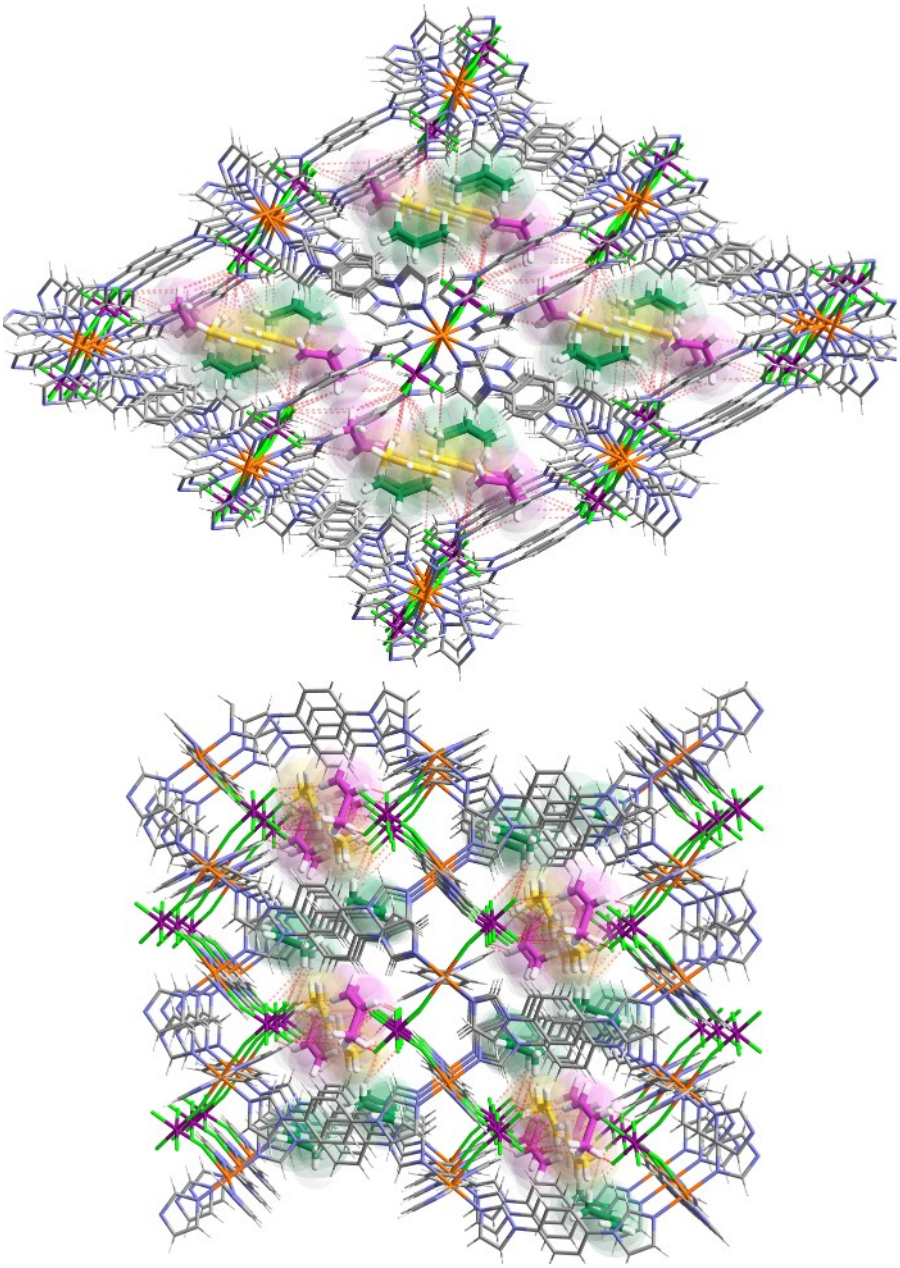

Figure S17. (Top) Top view and side view (bottom) of the periodic arrangement of C_3H_6 molecules in **SIFSIX-23-Cu⊃C_3H_6**.

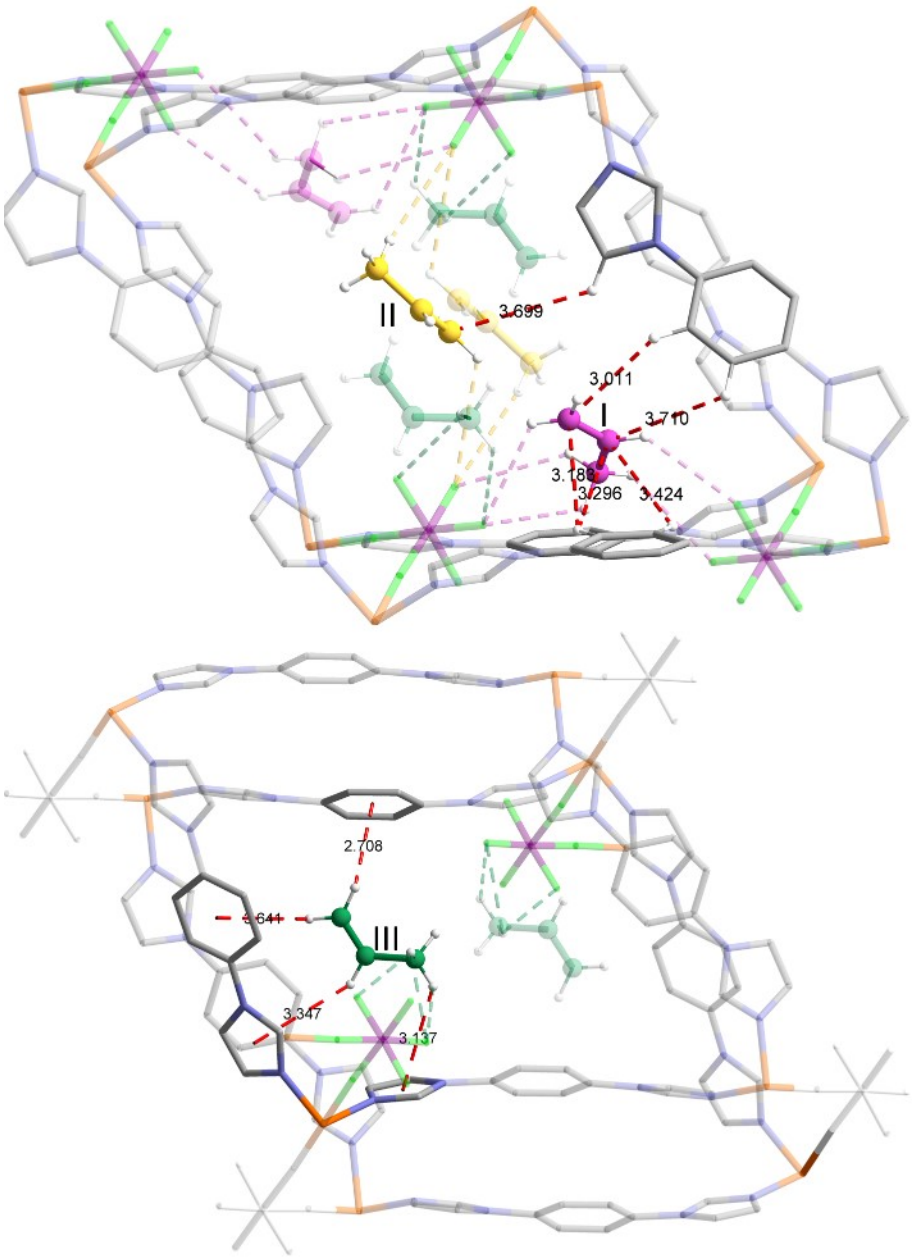

Figure S18. Other host-guest interactions stabilizing the C_3H_6 molecules (e.g., van der Waals forces, C-H···π interactions) in **SIFSIX-23-Cu⊃C_3H_6**.

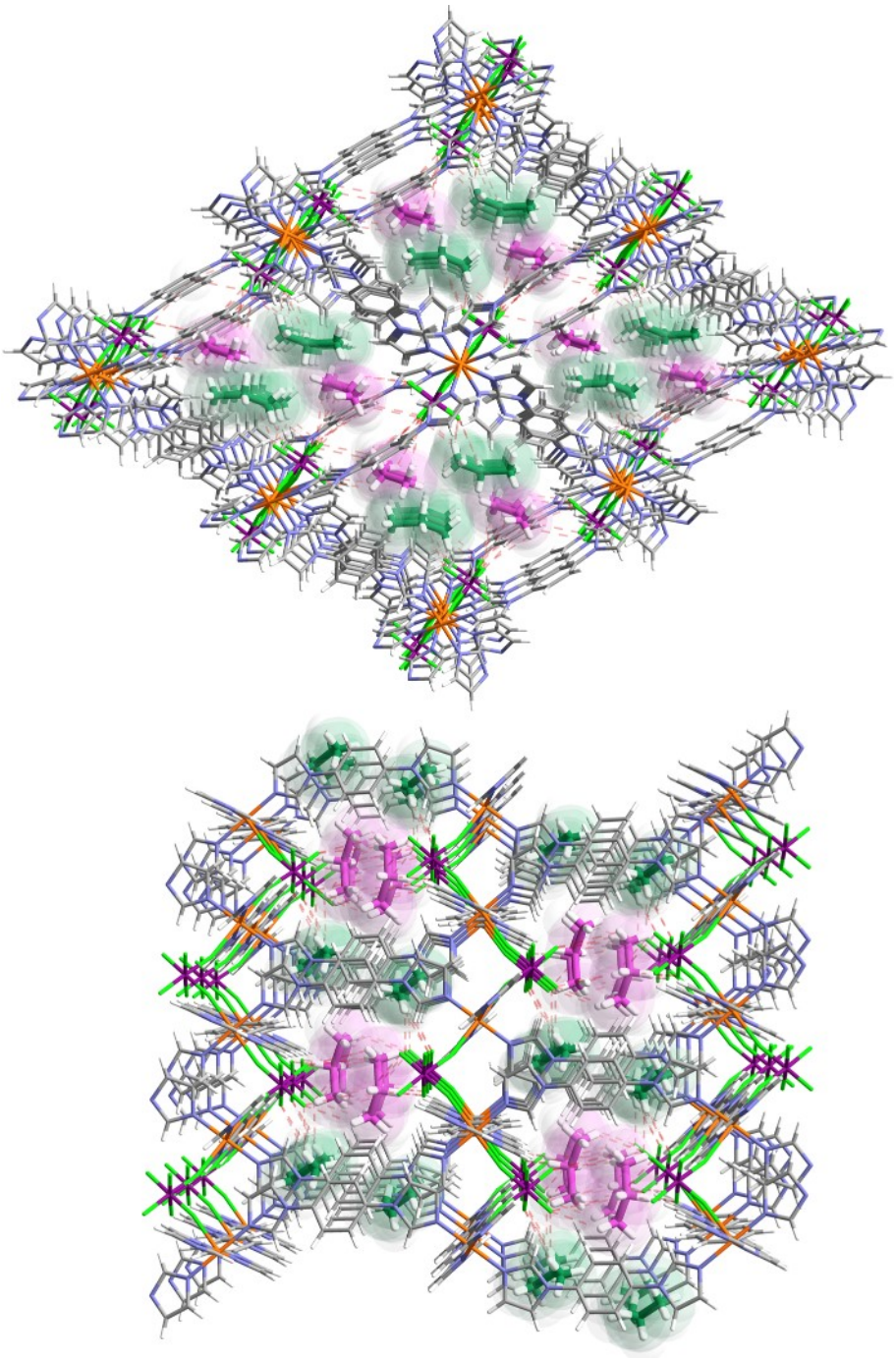

Figure S19. (Top) Top view and side view (bottom) of the periodic arrangement of C_3H_8 molecules in **SIFSIX-23-Cu⊃C_3H_8**.

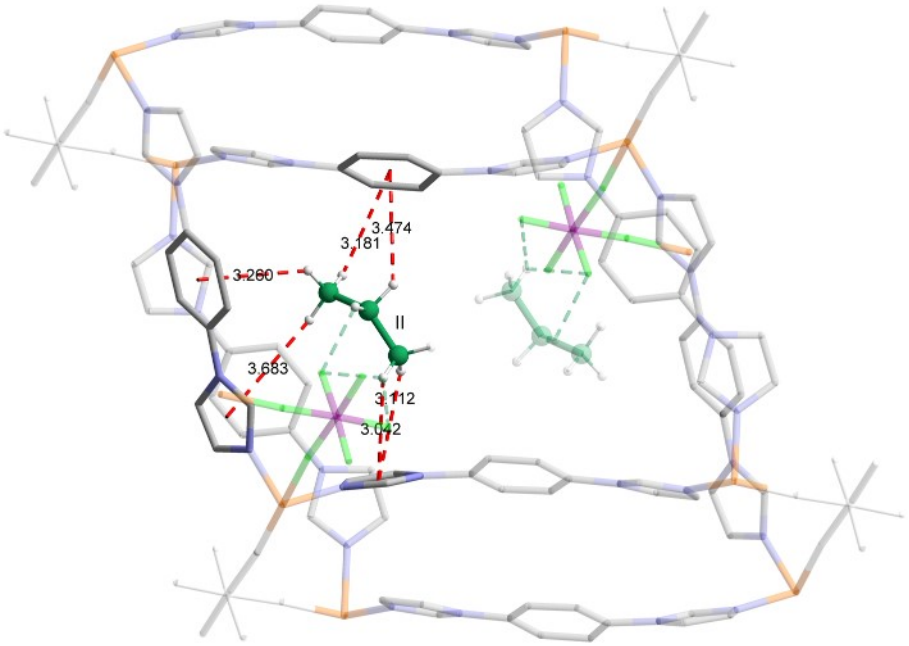

Figure S20. Other host-guest interactions stabilizing the C_3H_8 molecules (e.g., C-H···π interactions) in **SIFSIX-23-Cu⊃C_3H_8**.

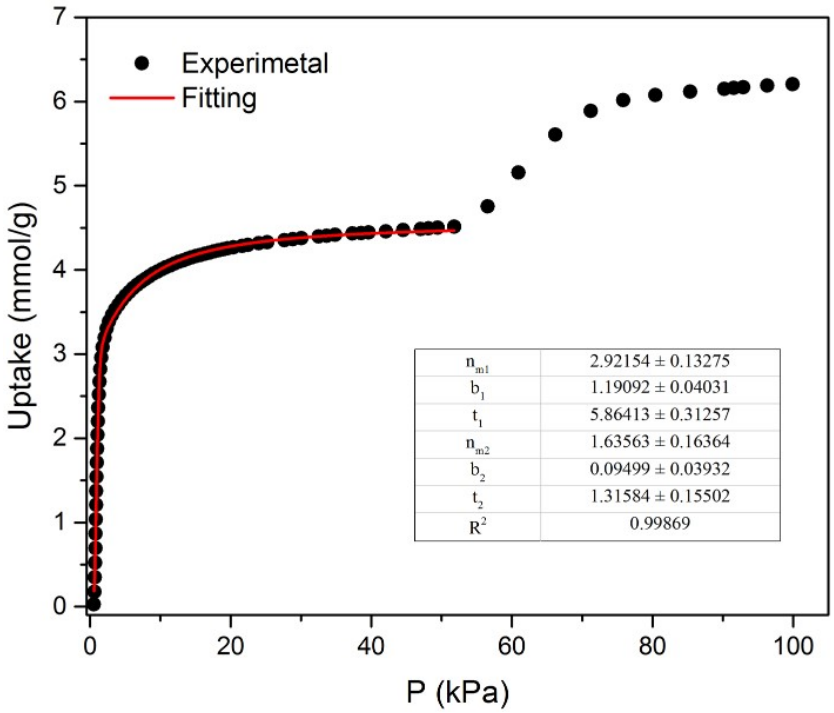

Figure S21. Dual-site Langmuir-Freundlich fitting of the C_3H_4 adsorption isotherm of **SIFSIX-23-Cu** at 273 K (0-30 kPa).

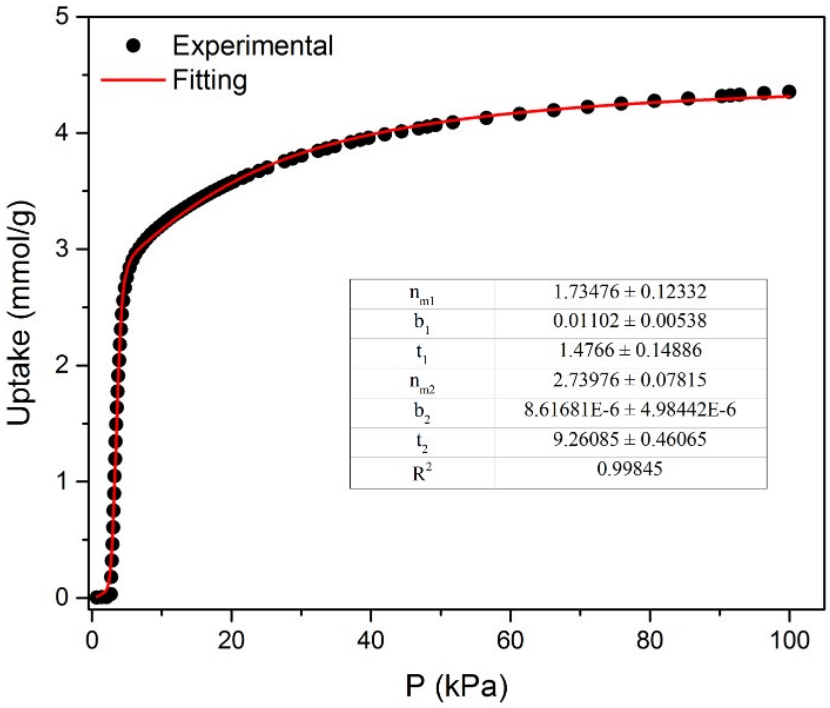

Figure S22. Dual-site Langmuir-Freundlich fitting of the C_3H_4 adsorption isotherm of **SIFSIX-23-Cu** at 298 K.

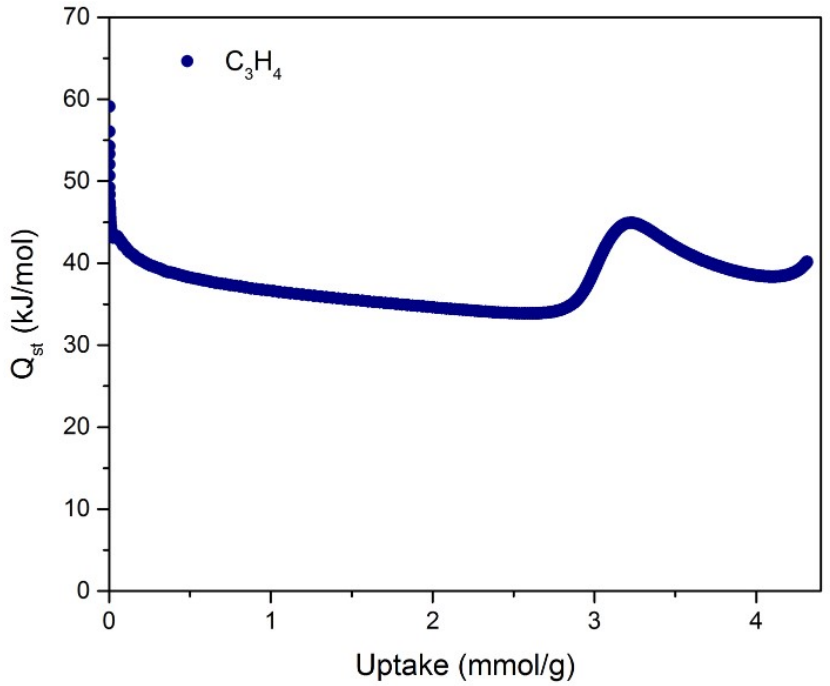

Figure S23. Estimated heat of adsorption of C_3H_4 in **SIFSIX-23-Cu**.

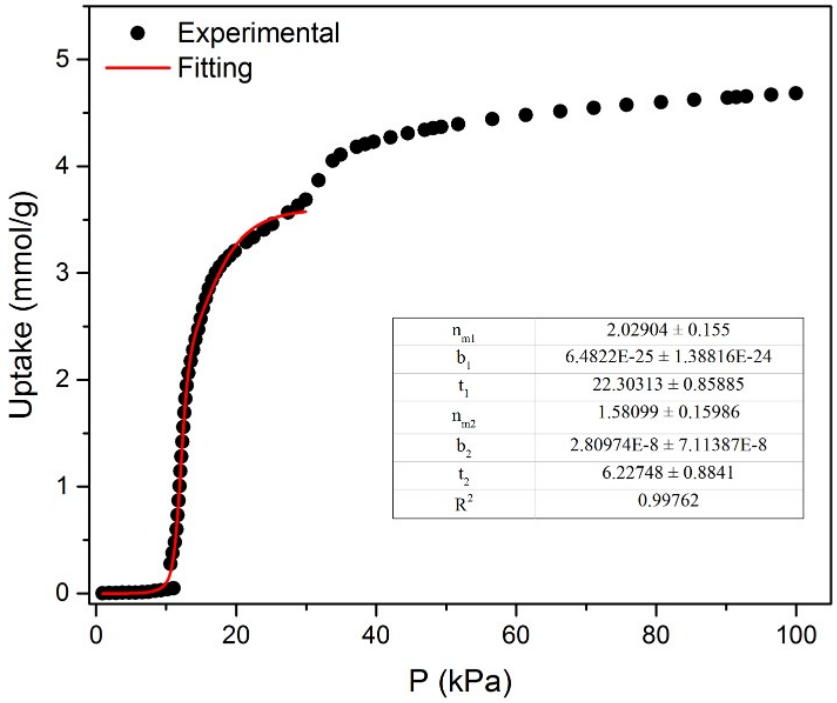

Figure S24. Dual-site Langmuir-Freundlich fitting of the C_3H_6 adsorption isotherm of **SIFSIX-23-Cu** at 273 K (0-30 kPa).

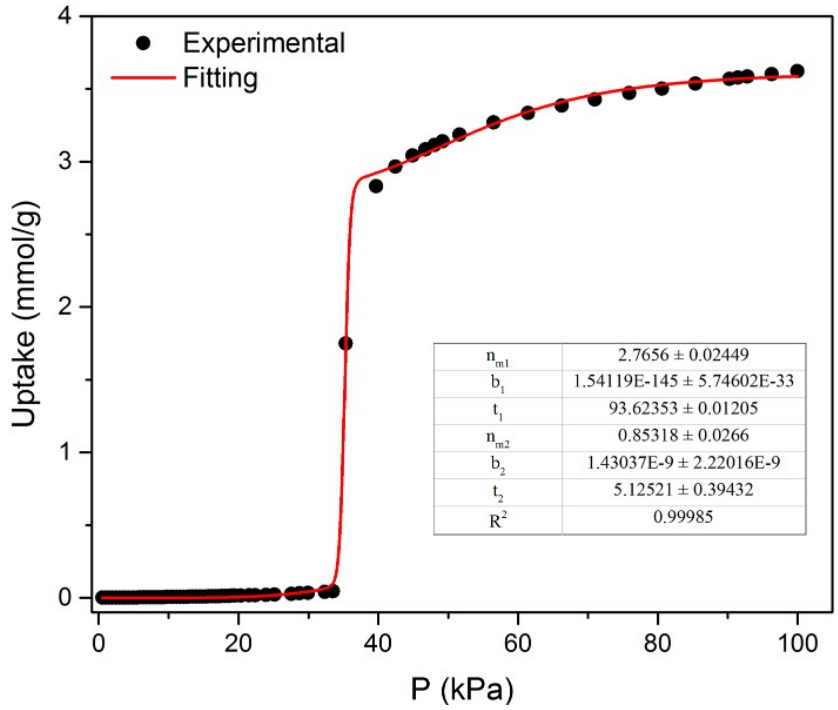

Figure S25. Dual-site Langmuir-Freundlich fitting of the C_3H_6 adsorption isotherm of **SIFSIX-23-Cu** at 298 K.

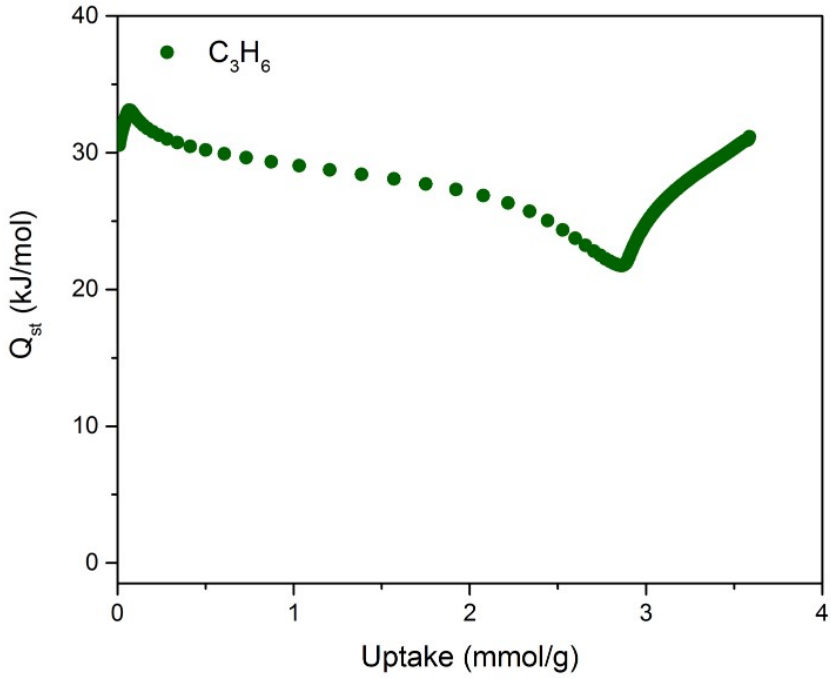

Figure S26. Estimated heat of adsorption of C_3H_6 in **SIFSIX-23-Cu**.

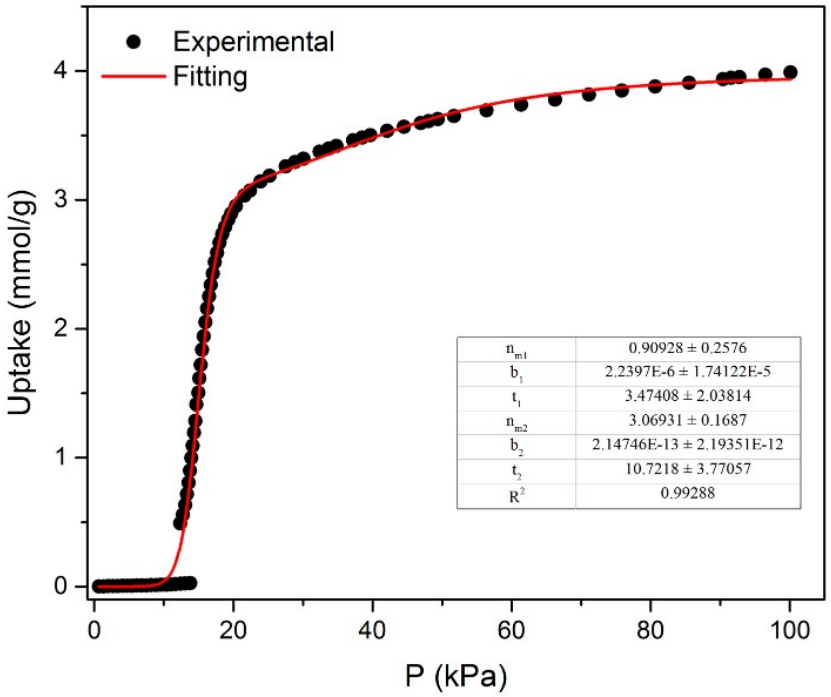

Figure S27. Dual-site Langmuir-Freundlich fitting of the C_3H_8 adsorption isotherm of **SIFSIX-23-Cu** at 273 K.

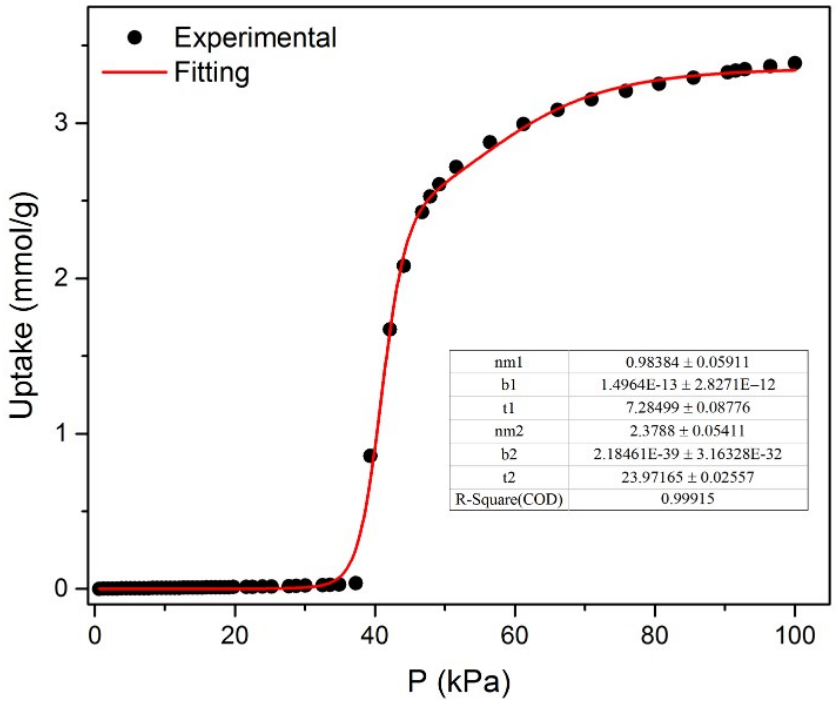

Figure S28. Dual-site Langmuir-Freundlich fitting of the C_3H_8 adsorption isotherm of **SIFSIX-23-Cu** at 298 K.

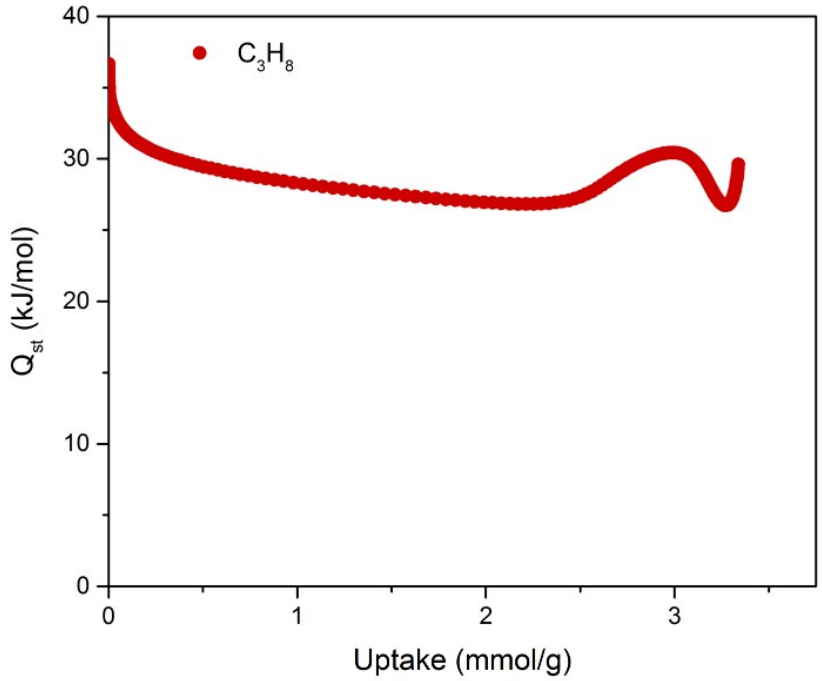

Figure S29. Estimated heat of adsorption of C_3H_8 in **SIFSIX-23-Cu**.

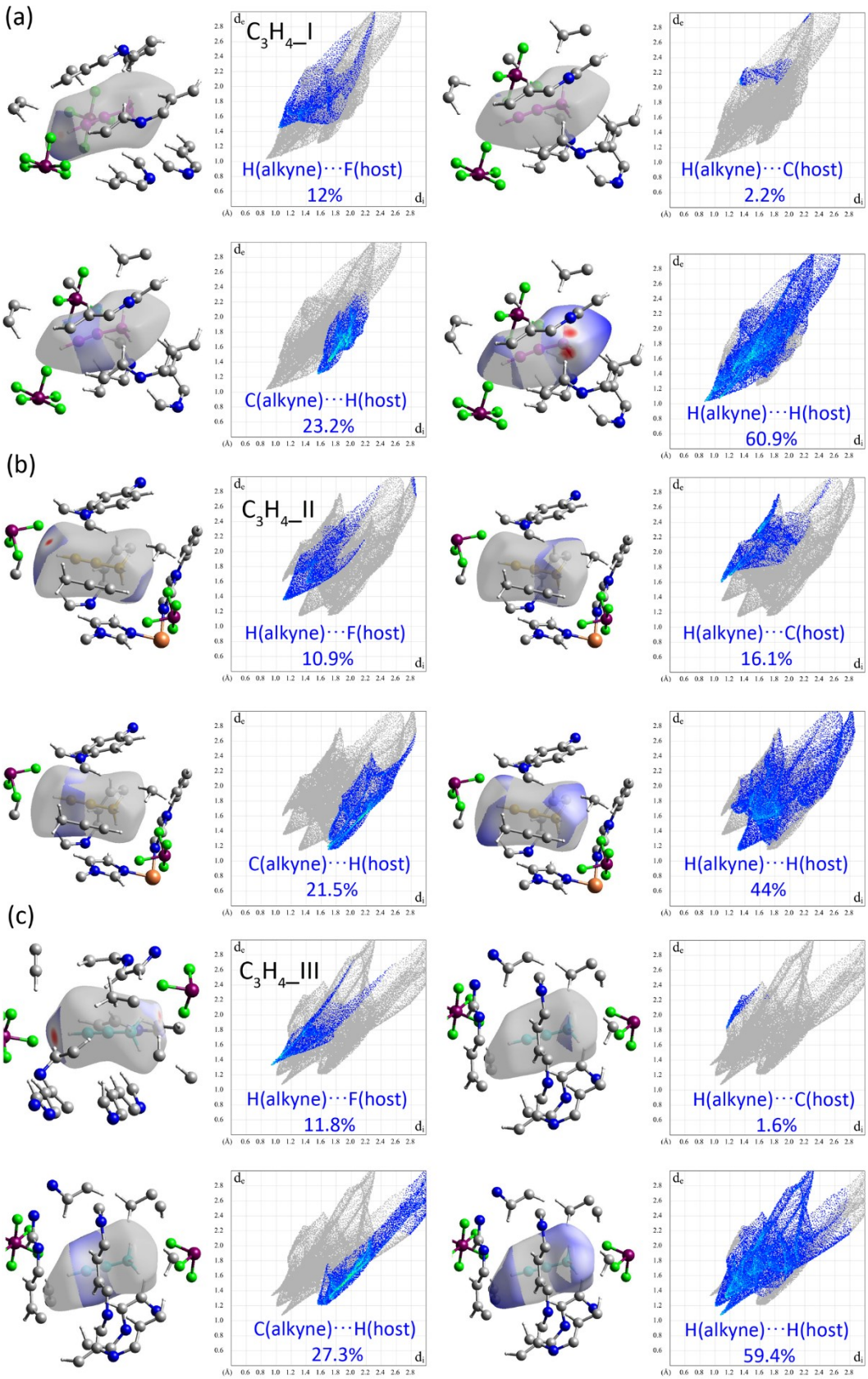

Figure S30. The decomposed 2D fingerprint plots and proportion for the H···F, H···C/ C···H and H···H contacts of different (I-III) C_3H_4 molecules on the Hirshfeld surfaces.

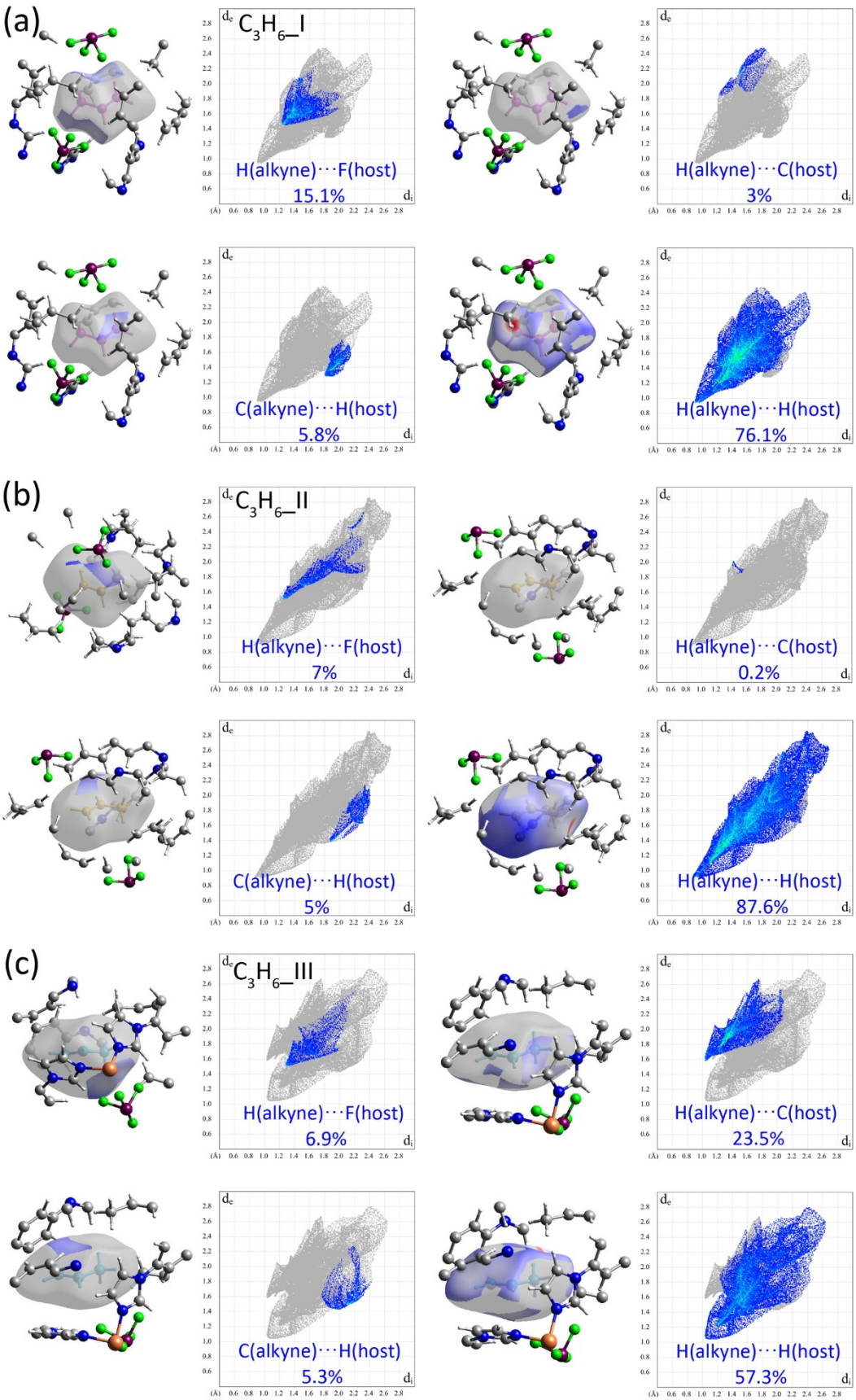

Figure S31. The decomposed 2D fingerprint plots and proportion for the H···F, H···C/ C···H and H···H contacts of different (I-III) C_3H_6 molecules on the Hirshfeld surfaces.

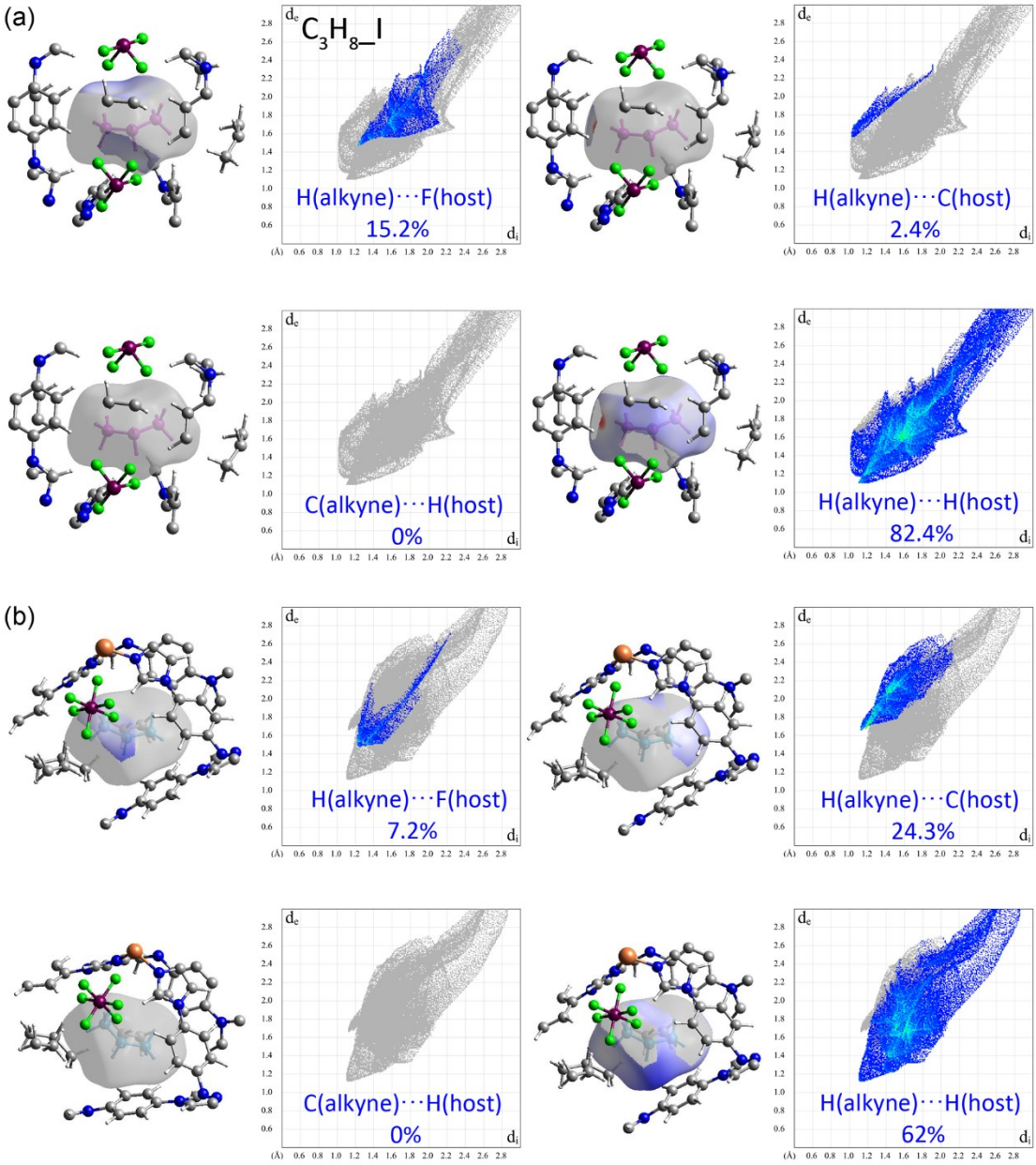

Figure S32. The decomposed 2D fingerprint plots and proportion for the H···F, H···C/ C···H and H···H contacts of different (I-III) C_3H_8 molecules on the Hirshfeld surfaces.

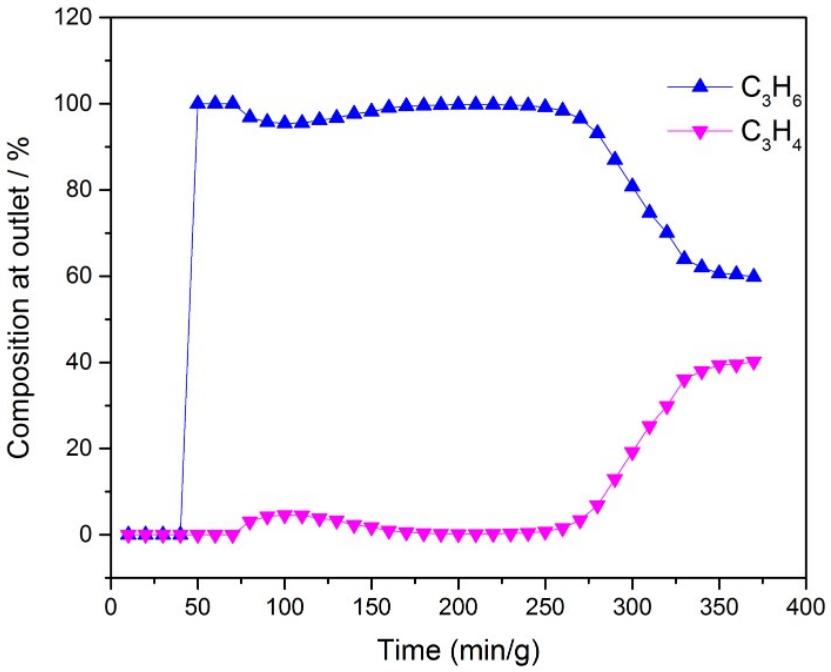

Figure S33. Instant outlet gas composition in breakthrough experiment using a mixture of C_3H_4/C_3H_6 (40:60, v/v) as inlet feed.

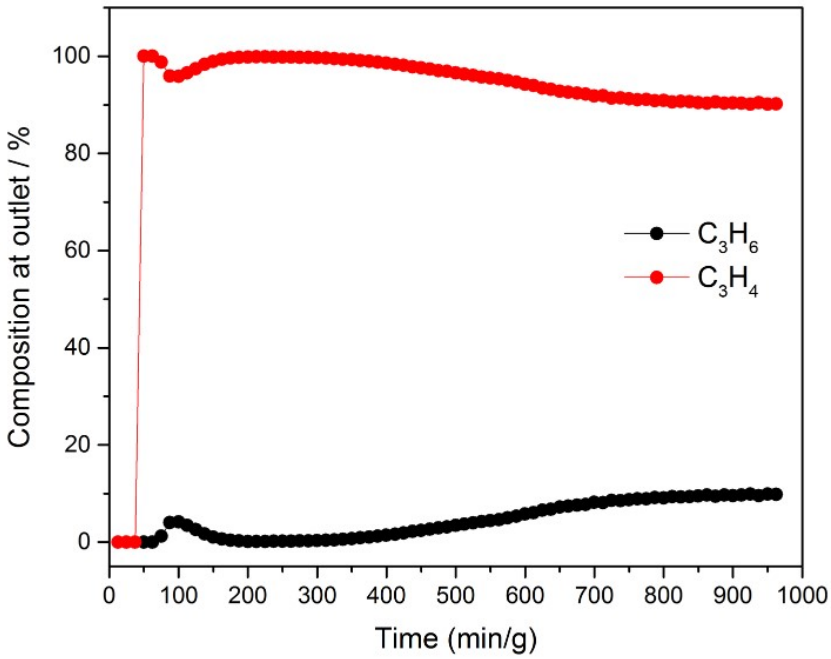

Figure S34. Instant outlet gas composition in breakthrough experiment using a mixture of C_3H_4/C_3H_6 (10:90, v/v) as inlet feed.

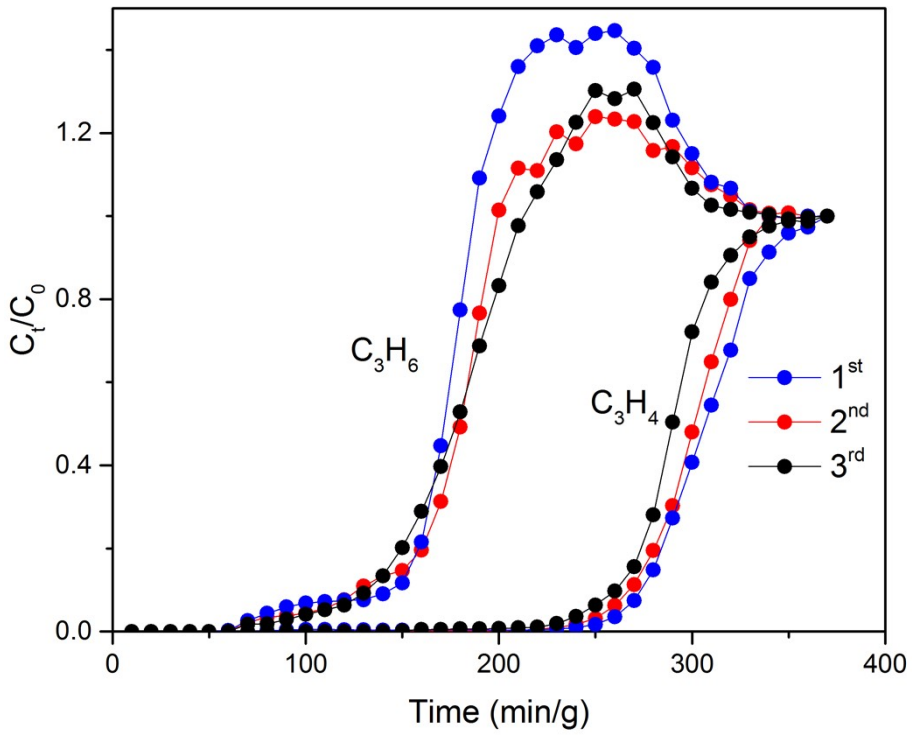

Figure S35. Three cycles of breakthrough experiments using a mixture of C_3H_4/C_3H_6 (40:60, v/v) as inlet feed. After each cycle, the gas-adsorbed sample was first flushed using He at 25 °C for a period of time, then the sample was heated to 100 °C to be fully activated.

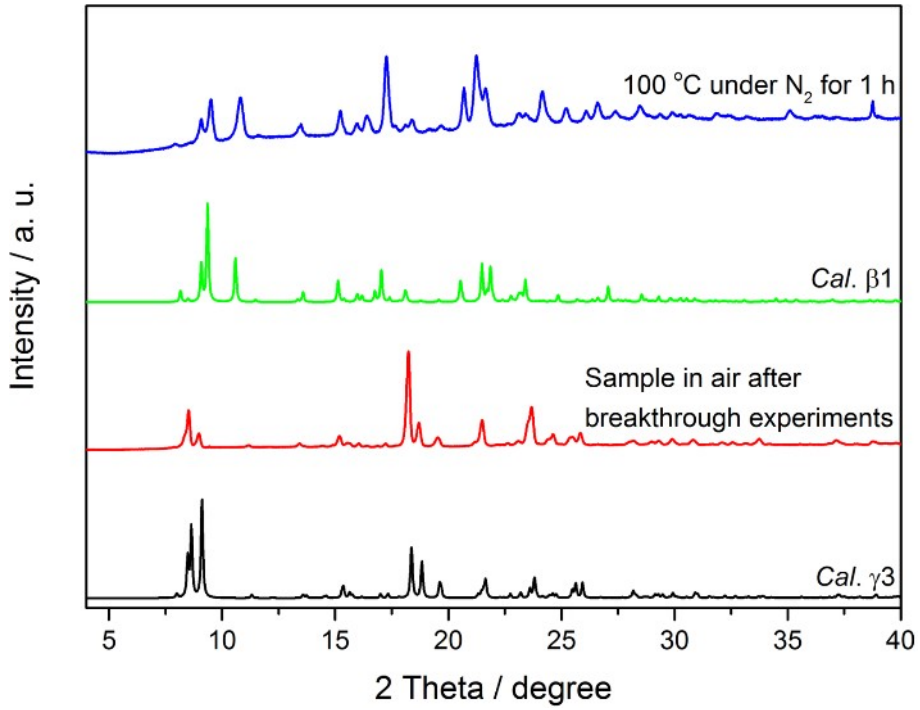

Figure S36. PXRD pattern for sample after breakthrough experiment. The regenerated sample in air will capture water in air to expand, which can be reactivated by heating, confirming the structure integrity after breakthrough experiment.

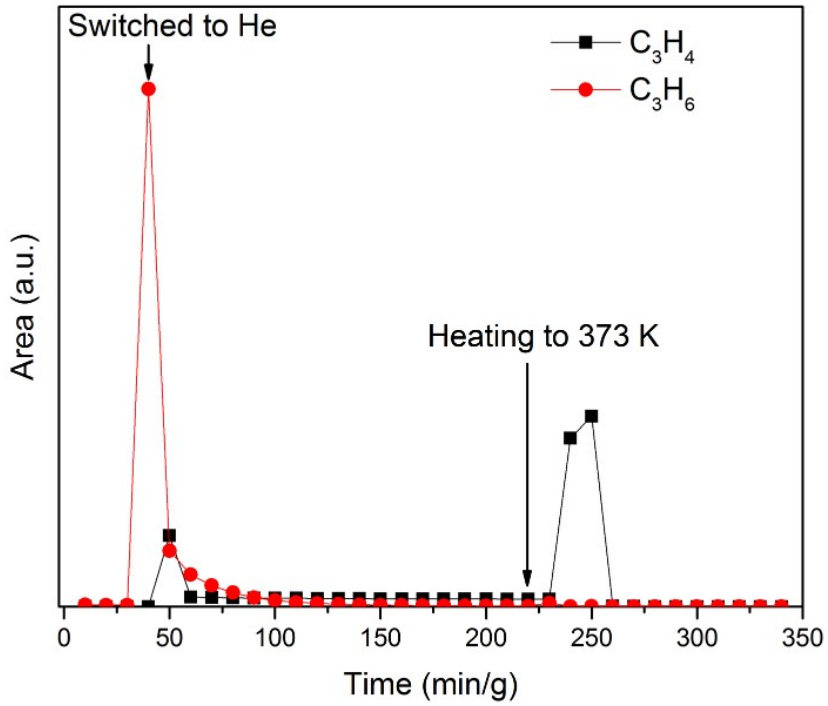

Figure S37. Desorption curves after the breakthrough experiment using a mixture of C_3H_4/C_3H_6 (10:90, v/v) as inlet feed. The gas-adsorbed sample was first flushed using He at 25 °C for a period of time, then the sample was heated to 100 °C. Note: the initial high concentration of C_3H_6 is ascribed to the gas residue in the pipe line and in the column (dead space), which cannot evidence the co-adsorption precisely.

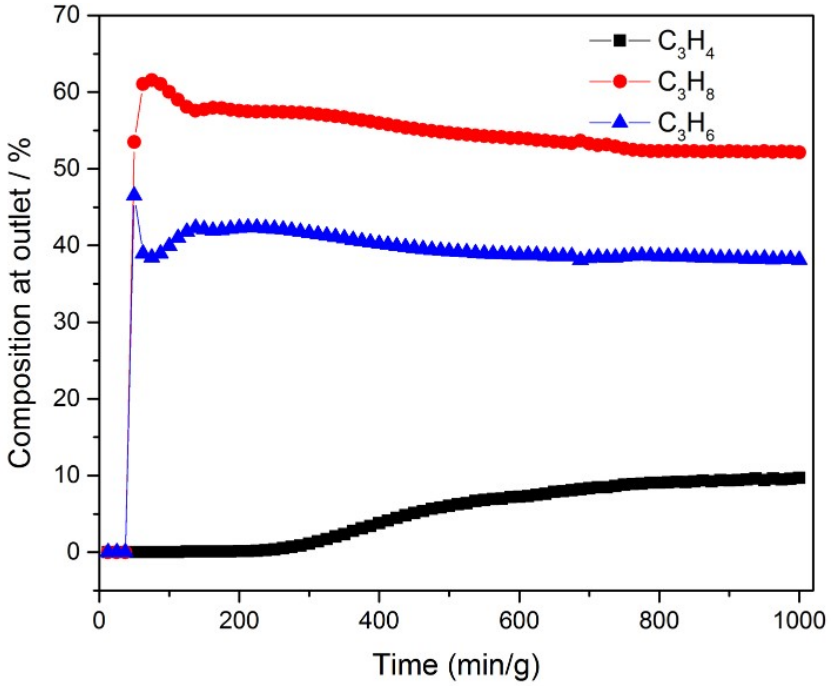

Figure S38. Instant outlet gas composition in breakthrough experiment using a mixture of

$C_3H_4/C_3H_6/C_3H_8$ (10:40:50, v/v/v) as inlet feed.

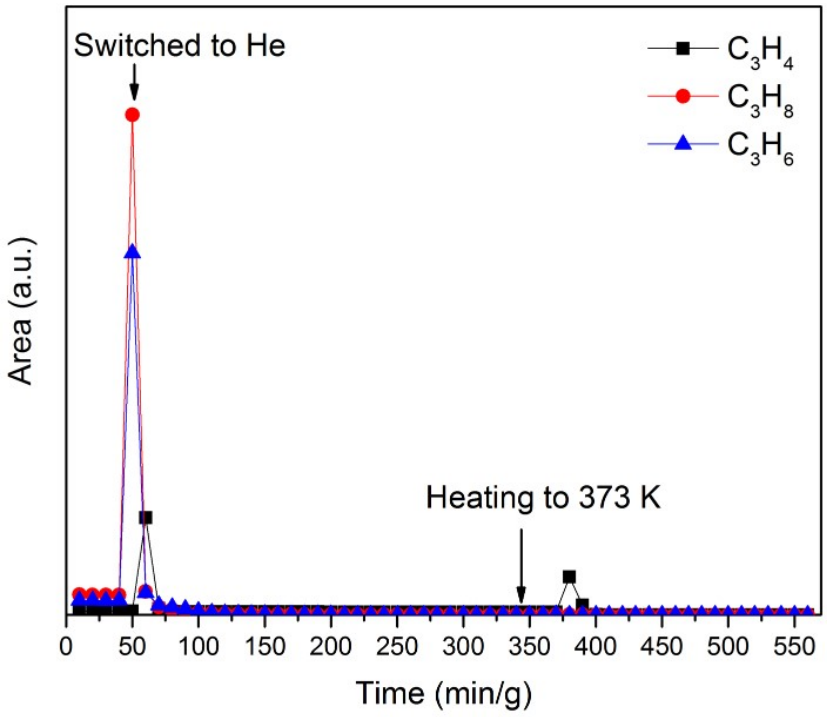

Figure S39. Desorption curves after the breakthrough experiment using a mixture of $C_3H_4/C_3H_6/C_3H_8$ (10:40:50, v/v/v) as inlet feed. The gas-adsorbed sample was first flushed using He at 25 °C for a period of time, then the sample was heated to 100 °C. Note: the initial high concentrations of C_3H_6 and C_3H_8 are ascribed to the gas residues in the pipe line and in the column (dead space), which cannot evidence the co-adsorption precisely.

9. Supporting Tables

Table S1. Crystallographic data and structure refinement summary for **SIFSIX-23-Cu (represented as '23' for short)**.

Compounds	**23⊃C_3H_4** (***Narrow-pore***)	**23⊃C_3H_6** (***Narrow-pore***)	**23⊃C_3H_8** (***Narrow-pore***)
Formula	$C_{30}H_{28}CuF_6N_8Si$	$C_{31.5}H_{35}CuF_6N_8Si$	$C_{28.5}H_{32}CuF_6N_8Si$
Formula weight	706.23	731.30	692.25
Temperature (K)	150	150	150
Crystal system	triclinic	triclinic	triclinic
Space group	*P*-1	*P*-1	*P*-1
a (Å)	12.3857(8)	12.4446(10)	12.4086(10)
b (Å)	12.4230(8)	12.9292(11)	12.7851(11)
c (Å)	13.1942(9)	13.3270(11)	13.5849(12)
α (deg)	63.892(3)	63.239(2)	65.814(2)
β (deg)	88.521(4)	70.955(2)	68.712(2)
γ (deg)	64.842(4)	63.228(2)	63.821(2)
V (Å^3)	1617.28(19)	1688.8(2)	1720.0(3)
Z	2	2	2
D_c (g·cm^{-3})	1.450	1.438	1.337
μ(mm^{-1})	1.920	0.751	0.733
R_{int}	0.0687	0.0543	0.0645
Data collected/unique	24053/6757	29252/5973	37550/6046
R_1 [$I > 2\sigma(I)$][a]	0.1433	0.1166	0.1172
wR_2 [all data][b]	0.3746	0.3215	0.3433
GOF	1.058	1.075	1.069

[a] $R_1 = \Sigma||F_o|-|F_c||/\Sigma|F_o|$. [b] $wR_2 = |\Sigma w(|F_o|^2-|F_c|^2)|/\Sigma|w(F_o^2)^2|^{1/2}$

Table S2. Comparison of unit cell parameters of different phases of **SIFSIX-23-Cu**

Compound	*a* (Å)	*b* (Å)	*c* (Å)	*α* (°)	*β* (°)	*γ* (°)	*V* (Å^3)	*Space group*
SIFSIX-23-Cu-β1	10.417	11.648	12.239	64.535	71.549	74.498	1256.8	*P-1*
SIFSIX-23-Cu-γ3	11.868	12.443	12.524	101.947	107.286	115.103	1475.7	*P-1*
SIFSIX-23-Cu-γ3[a]	11.868	12.443	12.524	101.947	72.714	64.897	1475.7	*P-1*
SIFSIX-23-Cu-γ2	12.197	12.507	12.568	60.721	79.864	64.958	1513.8	*P-1*
SIFSIX-23-Cu⊃C_3H_4	12.386	12.423	13.194	63.892	88.521	64.842	1617.3	*P-1*
SIFSIX-23-Cu⊃C_3H_6	12.445	12.929	13.327	63.239	70.955	63.228	1688.8	*P-1*
SIFSIX-23-Cu⊃C_3H_8	12.409	12.785	13.585	65.814	68.712	63.821	1720.0	*P-1*
SIFSIX-23-Cu-γ1	12.884	25.240	12.562	90	116.413	90	3658.7	*$P2_1/c$*
SIFSIX-23-Cu-α[c]	12.827	25.552	13.336	90	118.418	90	3844.0	*C2/m*

[a]The unit cell parameters were transformed using transformation matrix [1 0 0 0-1 0 0 0 -1], in order to get the unit cell angles to be acute. Please note that the three angles in the original unit cell are all larger than 90 degree, thus, even after transformation, one angle will still be larger than 90 degree (right-hand rule). Clearly, the different unit cell parameters of **SIFSIX-23-Cu-γ3** and **SIFSIX-23-Cu⊃C3H4** confirmed the difference between them, although the edges and diagonal distances of the parallelogram unit of the simplified CuL_2 **sql** net are similar.

Table S3. Comparative analysis of the structural differences between gas-loaded phases of **SIFSIX-23-Cu.** The fully open (**α**) and closed (**β1**) phases are provided for comparison.

		SIFSIX-23-Cu-β1	**SIFSIX-23-Cu⊃C_3H_4**	**SIFSIX-23-Cu⊃C_3H_6**
Coordination geometry	Bond length and bond angle	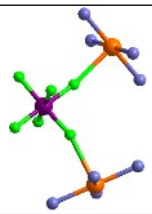		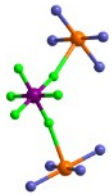
	Cu-F (Å)	2.3521(2)/2.3928(1)	2.3069(1)/2.3457(2)	2.4142(16)/2.3448 (18)
	Cu-N(*syn*) (Å)	2.0072(1)/1.9837(1)	1.9965(1)/2.0123(1)	2.0159(17)/2.0196(18)
	Cu-N(*anti*) (Å)	2.0069(1)/2.1046(2)	1.9915(1)/1.9985(2)	1.9815(18)/2.0260(14)
	Cu-Cu (Å)	6.1929(4)	6.2223(5)	6.4194(44)
	∠N-Cu-N (°)	88.304(5)-91.696(6)	88.326(5)-91.674(5)	87.384(65)-92.616(61)
	∠Cu-F-Si (°)	163.246(6)/168.274(6)	162.715(6)/169.088(6)	158.833(15)/170.012(86)
	∠Cu-Si-Cu (°)	99.894(3)	101.904(2)	104.672(34)
sql net formed by bi-imidazolyl ligands with equal amount of *syn*- and *anti*-conformers		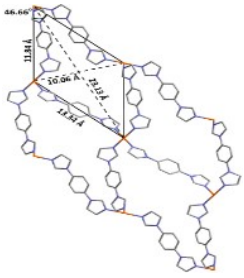	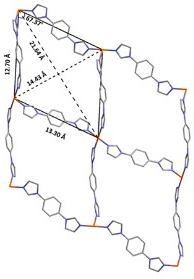	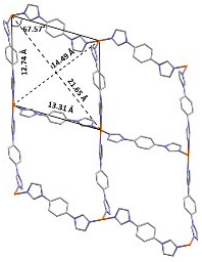
Parallelogram formed by bi-imidazolyl ligands with equal amount of *syn*- and *anti*-conformers		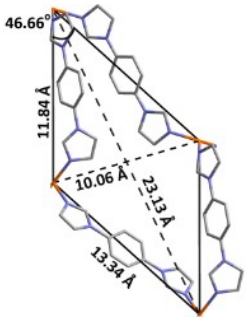	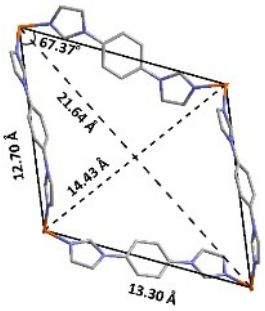	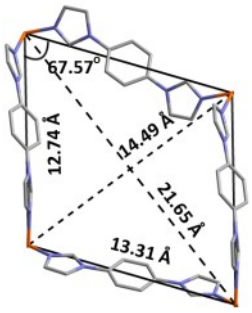
Dihedral angles between imidazolyl plane and phenyl plane of ligands 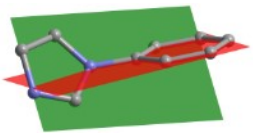		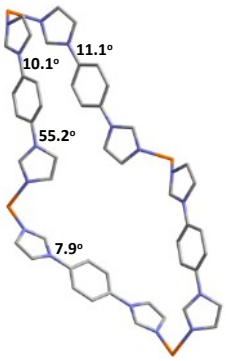	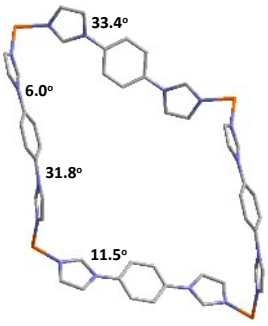	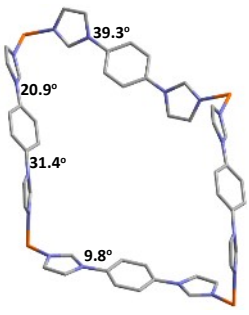
		SIFSIX-23-Cu-β1	**SIFSIX-23-Cu⊃C_3H_4**	**SIFSIX-23-Cu⊃C_3H_6**

Angle between C_{phenyl}-$N_{imidazolyl}$ covalent bond and imidazolyl plane 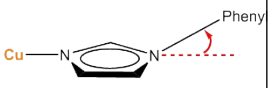	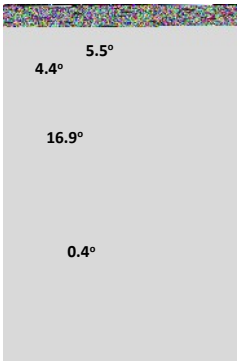	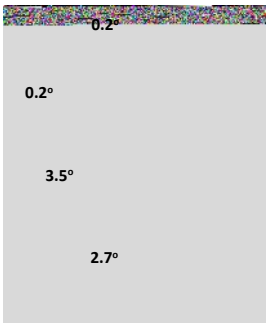	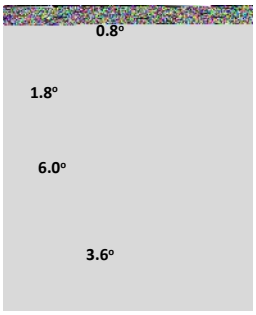
Angle between Cu-N coordination bond and imidazolyl plane 	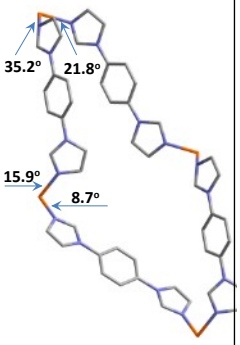	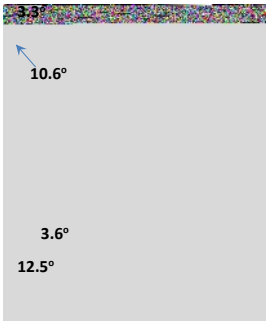	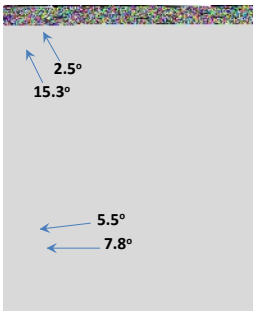
Dihedral angles between imidazolyl plane (blue plane) and Cu atoms plane (light blue one) 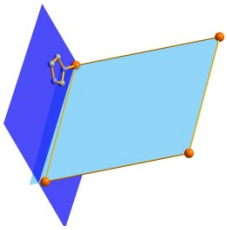	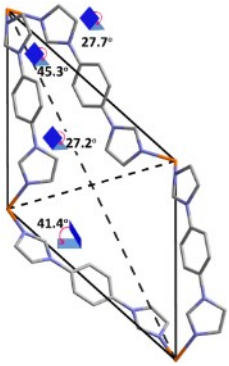	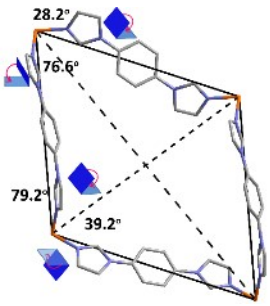	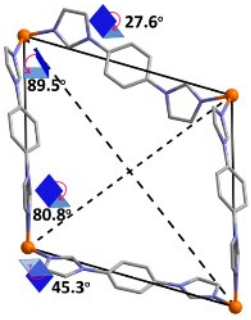
3D nets with *syn*-conformational ligands highlighted in black	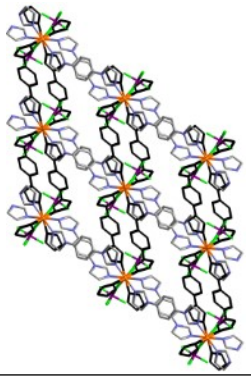	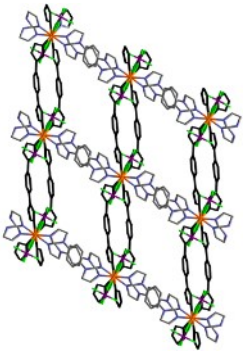	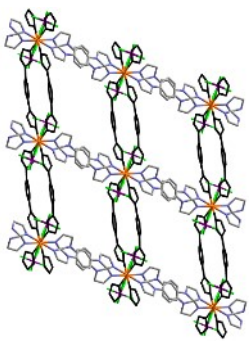

		SIFSIX-23-Cu⊃C_3H_8	SIFSIX-23-Cu-α
Coordination geometry	Bond length and bond angle		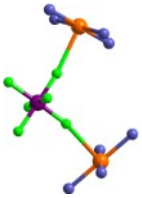
	Cu-F (Å)	2.2961(2)/2.3579(2)	2.4566(2)
	Cu-N(*syn*) (Å)	1.9927(1)/2.0003(1)	1.9907(2)
	Cu-N(*anti*) (Å)	2.0002(2)/2.0066(1)	1.9961(3)
	Cu-Cu (Å)	6.2043(5)	6.4014(9)
	∠N-Cu-N (°)	88.554(7)-91.446(6)	89.343(5)/90.657(5)
	∠Cu-F-Si (°)	163.789(10)/168.22(1)	168.489(6)
	∠Cu-Si-Cu (°)	101.339(4)	102.303(3)
sql net formed by bi-imidazolyl ligands with equal amount of *syn*- and *anti*-conformers		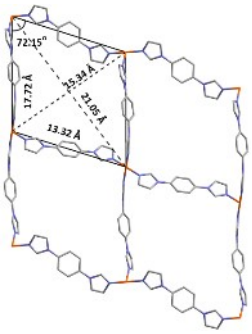	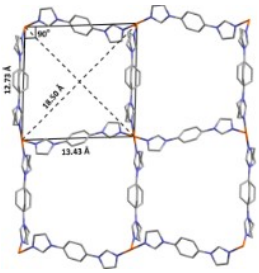
Parallelogram formed by bi-imidazolyl ligands with equal amount of *syn*- and *anti*-conformers		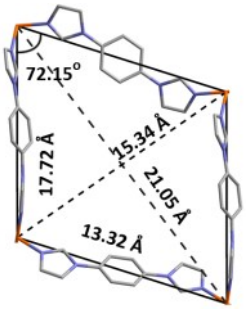	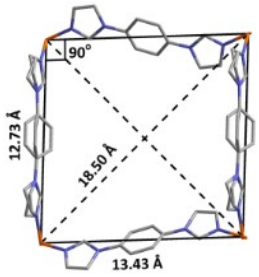
Dihedral angles between imidazolyl plane and phenyl plane of ligands		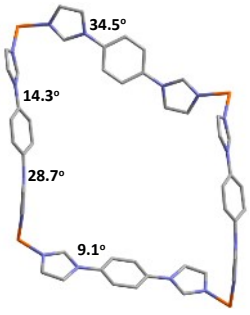	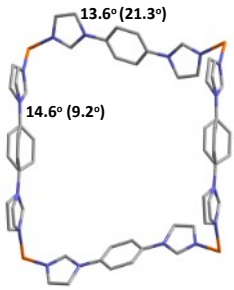

	SIFSIX-23-Cu⊃C_3H_8	SIFSIX-23-Cu-α
Angle between C_{phenyl}-$N_{imidazolyl}$ covalent bond and imidazolyl plane 	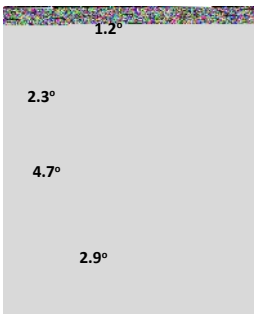	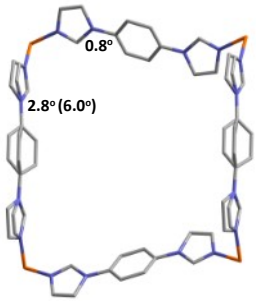
Angle between Cu-N coordination bond and imidazolyl plane 	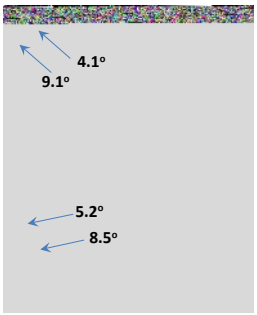	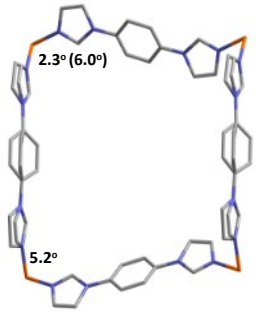
Dihedral angles between imidazolyl plane (blue plane) and Cu atoms plane (light blue plane)	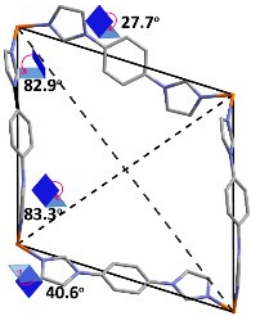	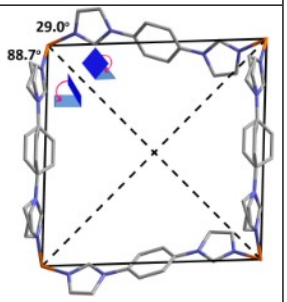
3D nets with *syn*-conformational ligands highlighted in black	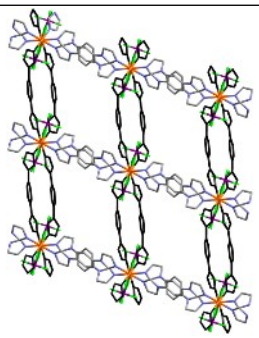	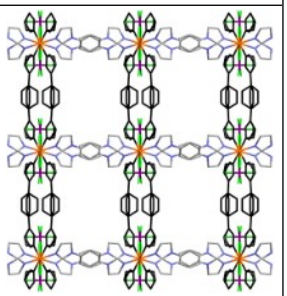

Table S4. Possible C(aromatic)-H···F hydrogen bonds with $d_{F\cdots H}$ < 2.8 Å (short F···H contacts)

SIFSIX-23-Cu-α	**SIFSIX-23-Cu⊃C_3H_4**
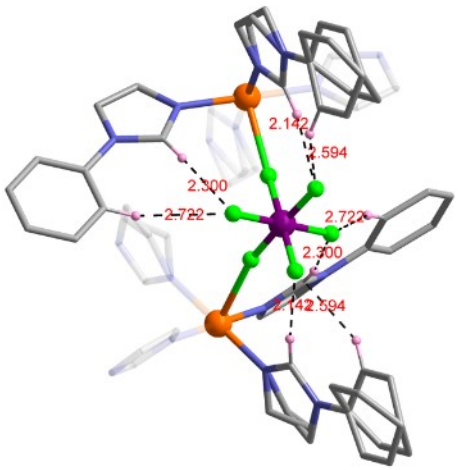	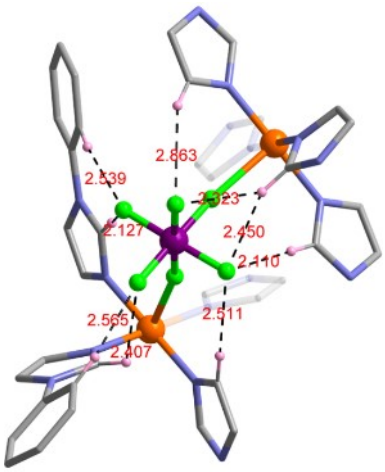
SIFSIX-23-Cu⊃C_3H_6	**SIFSIX-23-Cu⊃C_3H_8**
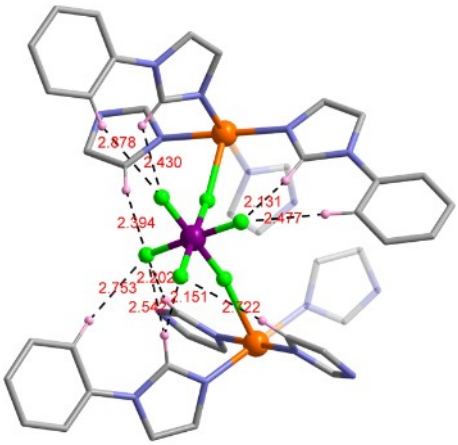	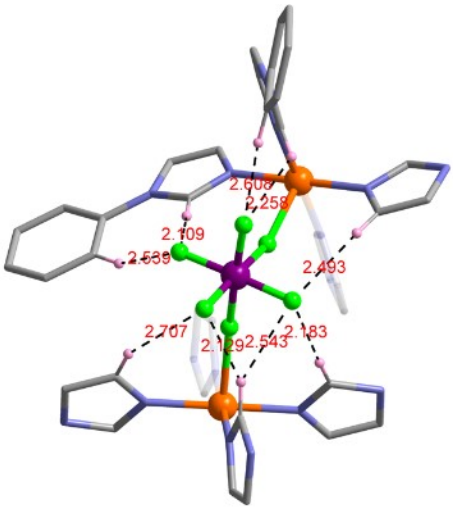
SIFSIX-23-Cu-β1	
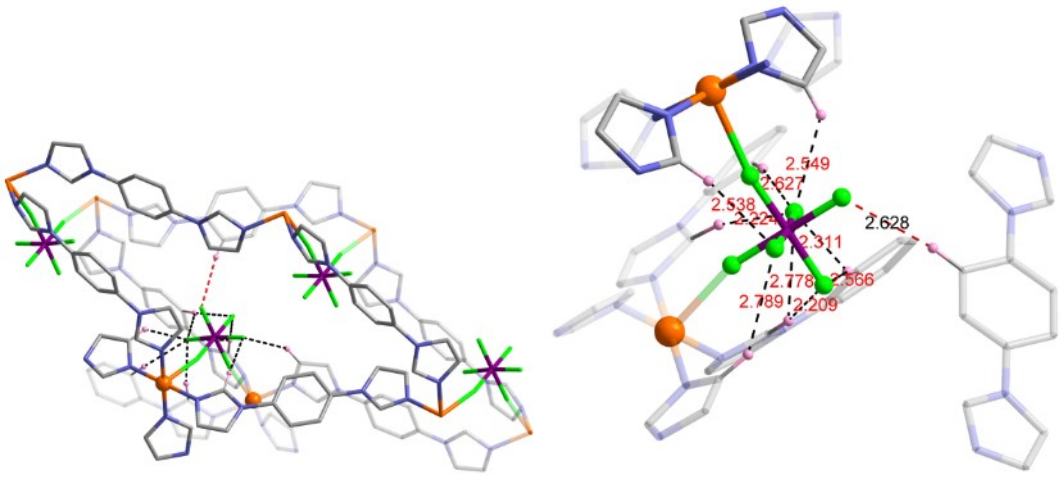	

1. C-H···F hydrogen bonds[13]: the black and red dash lines represent the hydrogen bonds

between SIFSIX and organic ligands which share the same Cu ions with SIFSIX anions. The red one represent the hydrogen bonds between SIFSIX and organic ligands which don't share the same Cu ion with SIFSIX anions. These hydrogen bonds can be considered to lock or stabilize the structure.

2. The acidity of hydrogen donor from the 2-positioned carbon atom on the imidazolyl ring is high because the strong electron-withdrawing ability of the two bonded nitrogen atoms and the coordinated copper ions can increase the C-H acidity,[14] therefore, the hydrogen bonds between $C_{imidazolyl}(2)$-H···F are shorter in lenghth and stronger in strength compared with others.

10. References

[1] B.-Q. Song, Q.-Y. Yang, S.-Q. Wang, M. Vandichel, A. Kumar, C. Crowley, N. Kumar, C.-H. Deng, V. GasconPerez, M. Lusi, H. Wu, W. Zhou, M. J. Zaworotko, *J. Am. Chem. Soc.* **2020**, *142*, 6896-6901.

[2] a) G.-S. Yang, H.-Y. Zang, Y.-Q. Lan, X.-L. Wang, C.-J. Jiang, Z.-M. Su, L.-D. Zhu, *CrystEngComm* **2011**, *13*, 1461-1466; b) J. Fan, L. Gan, H. Kawaguchi, W.-Y. Sun, K.-B. Yu, W.-X. Tang, *Chem. - Eur. J.* **2003**, *9*, 3965-3973.

[3] Version 2017.3-0 ed., APEX3. Bruker AXS Inc., Madison, Wisconsin, USA, **2017**.

[4] Version 2014/4 ed., SADABS. Bruker AXS Inc., Madison, Wisconsin, USA, **2014**.

[5] Version 2014/2 ed., XPREP. Bruker AXS Inc., Madison, Wisconsin, USA, **2014**.

[6] G. Sheldrick, *Acta Cryst. A* **2015**, *71*, 3-8.

[7] G. Sheldrick, *Acta Cryst. C* **2015**, *71*, 3-8.

[8] O. V. Dolomanov, L. J. Bourhis, R. J. Gildea, J. A. K. Howard, H. Puschmann, *J. Appl. Crystallogr.* **2009**, *42*, 339-341.

[9] A. L. Spek, *Acta Cryst. C* **2015**, *71*, 9-18.

[10] A. L. Spek, *Acta Cryst. D* **2009**, *65*, 148-155.

[11] K.-J. Chen, D. G. Madden, T. Pham, K. A. Forrest, A. Kumar, Q.-Y. Yang, W. Xue, B. Space, J. J. Perry IV, J.-P. Zhang, X.-M. Chen, M. J. Zaworotko, *Angew. Chem. Int. Ed.* **2016**, *55*, 10268-10272.

[12] H. Pan, J. A. Ritter, P. B. Balbuena, *Langmuir* **1998**, *14*, 6323-6327.

[13] a) G. R. Desiraju, *Acc. Chem. Res.* **2002**, *35*, 565-573; b) J. L. Alonso, S.

Antolínez, S. Blanco, A. Lesarri, J. C. López, W. Caminati, *J. Am. Chem. Soc.* **2004**, *126*, 3244-3249; c) E. Kryachko, S. Scheiner, *J. Phys. Chem. A* **2004**, *108*, 2527-2535; d) W. Caminati, J. C. López, J. L. Alonso, J.-U. Grabow, *Angew. Chem. Int. Ed.* **2005**, *44*, 3840-3844.

[14] a) O. Karagiaridi, M. B. Lalonde, W. Bury, A. A. Sarjeant, O. K. Farha, J. T. Hupp, *J. Am. Chem. Soc.* **2012**, *134*, 18790-18796; b) M. B. Lalonde, O. K. Farha, K. A. Scheidt, J. T. Hupp, *ACS Catal.* **2012**, *2*, 1550-1554.